International workshop on
overflowing erosion of dams and dikes
Concrete Dams Overtopping Erosion
Sesion 6: State of the Art Part - 1

Aussois, France, 11- 14 December 2017

Technical University of Cartagena Research.
Study Cases: Paute Cardenillo and Toachi Dams

Luis G. Castillo and José M. Carrillo
[1]Dept. of Civil Engineering
Universidad Politécnica de Cartagena (UPCT)
Paseo Alfonso XIII, 52, 30203 Cartagena
Spain
E-mail: luis.castillo@upct.es, jose.carrillo@upct.es

ABSTRACT

The increasing of the magnitude of design floods has prompted the re-evaluations of spillway capacity and the operational scenarios for large dams throughout the world. Current capacity of many spillways is inadequate and dams might be overtopped during extreme events. New loading for the dam and questions about erosion and scour downstream from the dam are necessary. In this way we need to estimate the hydrodynamic actions on the dam bottom or the basin where the jet discharges, as a function of the characteristics of the jet. So the pressure and velocity distributions of the flow in the plunge pool must be estimated to evaluate potential scour that might destabilize the dam. The high turbulence and aeration phenomena that appear in falling jets and dissipation basins make it difficult to carry out studies based only on classical methodologies. This work addresses overtopping flows, and compares numerical results against our own experiments. Instantaneous pressures, velocities and air entrainment were obtained with the use of piezoresistive transducers, Acoustic Doppler Velocimeter and optical fiber, respectively. Mean velocity field and turbulence kinetic energy profiles were determined. To identify the level of reliability of models, numerical simulations were carried out by using the "homogeneous" model of ANSYS CFX, together with different turbulence closures.

In this paper we also present two Study Cases: Paute - Cardenillo (arch dam of 135 m height) and Toachi (gravity dam of 59 m height). To evaluate the stability and safety of the structures, it is necessary to ascertain the shape and dimensions of the scour generated downstream from the dams. We studied the scour, due to the operation of the free surface spillway and half-height outlets (Paute-Carenillo dam) with three complementary procedures: empirical formulae obtained in models and prototypes, semi-empirical methodology based on pressure fluctuations-erodibility index and computational fluid dynamics simulations (Flow-3D). A pre-excavated basin is proposed in Paute-Cardenillol dam and the velocities and pressures are analyzed. In the case the of the Toachi dam sky jump, in addition to the three previous procedures, a physical model 1:50 scale was carried out. The results demonstrated the suitability of combining different methodologies to achieve an adequate resolution of this complex phenomenon.

Keywords: Overtopping, Free Falling Jets, Air Entrainment, Numerical Simulations, Turbulence model, Scour.

1. INTRODUCTION

In recent years, the increasing magnitude of design floods has prompted re-evaluations of spillway capacity and operational scenarios for large dams throughout the world. Current capacity of many spillways is inadequate, raising the possibility that dams might be overtopped during extreme events. This creates new loading scenarios for the dam and raises questions about erosion and scour downstream from the dam (Wahl et al. 2008, FEMA 2014).

When the rectangular jet or nappe flow occurs due to overtopping, the design considerations need to ensure that most energy is dissipated, and that there is minimal to no erosion downstream of the dam. In other words, we need to estimate the hydrodynamic actions on the bottom of the basin where the jet discharges, as a function of the characteristics of the jet (Annandale 2006). The energy dissipation mechanisms that occur in the jet-basin structure can be grouped into the following: (a) aeration and disintegration of the jet in its fall, (b) air entrainment and diffusion of the jet into the basin, (c) impact on the basin bottom, and (d) recirculation in the basin (Figure 1).

Two of the variables needed to be defined in the design of the jets are the issuance conditions and the impingement conditions.

Issuance conditions correspond to the flow conditions at a location where the jet leaves the spillway and starts falling freely. In the illustrated arch dam case (inclined-crest), $z = -h$, where z is the vertical coordinate with origin in the crest weir, and h is the weir head. Similarly, in the gravity dam case (flat-topped) is also considered $z = -h$. The impingement conditions correspond to the jet section before the impact with the water surface of the basin. In this location, the mean velocity, V_j, and the impingement jet thickness, B_j, must be defined (see Figure 1).

This jet thickness must include the basic thickness due to gravity B_g, and the symmetric jet lateral spreading due to turbulence and aeration effects, ξ (Castillo 2006, Castillo et al. 2015):

$$B_j = B_g + 2\xi = \frac{q}{\sqrt{2gH}} + 4\varphi\sqrt{h}\left(\sqrt{2H} - 2\sqrt{h}\right) \tag{1a}$$

where q is the specific flow, H the fall height, and h is the energy head at the crest weir. $\varphi = K_\varphi T_u$, with T_u being the turbulence intensity (0.012 for arch dam and 0.013 for a gravity dam) and K_φ an experimental parameter (1.14 for circular jets, 1.24 for the overtopping on arch dam and 1.20 for the overtopping on a gravity dam).

By the way, in the case of gravity dam (flat-topped) the overtopping is produced on the crest of the dam through critical flow conditions. In the brink the depth is approximately $0.715\ y_c$ (Rouse 1936 and Wahl et al. 2008). However, as already indicated, the issuance conditions are considered at $z = -h$. Figures 1a and 1b show the overtopping on an arch dam (inclined-crest) and a gravity dam (flat-topped), respectively. When the jet falls through a long-enough distance, the jet becomes fully developed (L_b).
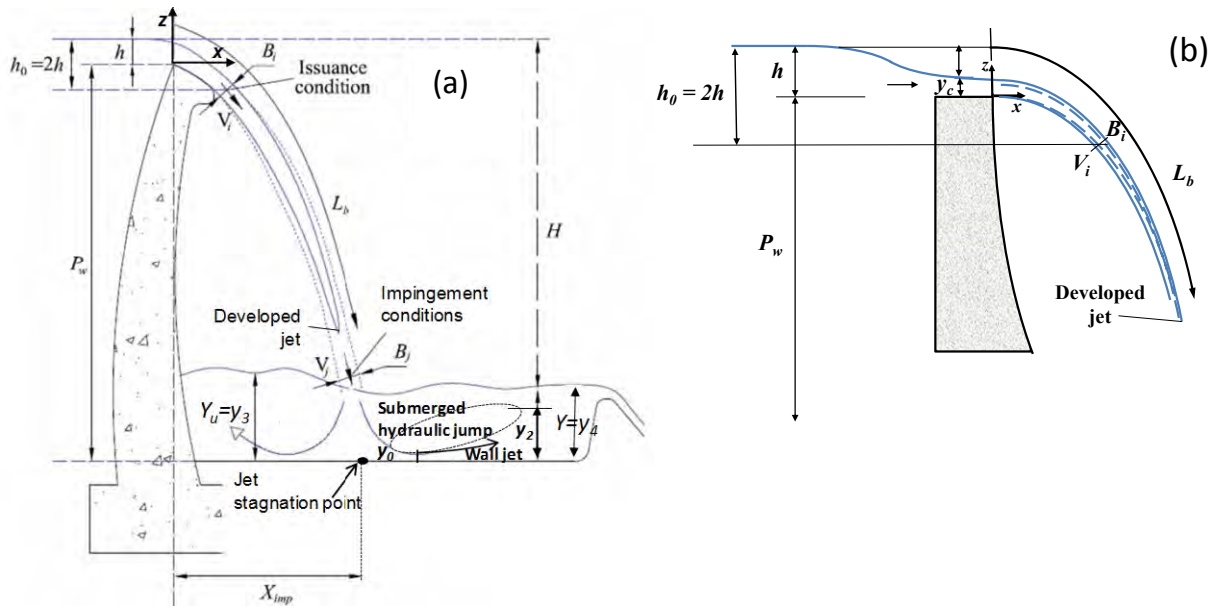
Figure 1. Schematic of falling rectangular jets and receiving basin. (a) Overtopping on an arch dam. (b) Overtopping on a gravity dam (Castillo and Carrillo 2016a).

Castillo (2006) and Castillo et al. (2015) established different equations to calculate the jet energy dissipation in the air and in the water cushion, as a function of the Y/B_j and H/L_b ratios (where Y and H denote the depth of the water cushion at the exit and the total head, respectively, and L_b is the break-up length). Castillo et al. (2015) proposed the following expression for estimating the break-up length:

$$\frac{L_b}{B_i F_i^2} = \frac{K}{(\varphi F_i^2)^{0.82}} \tag{1.b}$$

where B_i and F_i are the jet thickness and the Froude number in issuance conditions, respectively. K is an adjustment coefficient and that in the arch dam case is 0.85. If in the expression (1.b) we replacement the jet thickness $B_i = q / V_i$; velocity $V_i = 2\sqrt{gh}$; specific flow $q = h^{3/2}C_d$; Froude number $F_i = V_i/\sqrt{gB_i}$ and we solve for the break-up length, then it is obtained that (Castillo and Carrillo, 2016a):

$$L_b = \frac{C_d^{0.82}h^{0.73}}{2g^{0.68}\varphi^{0.82}}K \tag{1.c}$$

where C_d is the discharge coefficient (2.1 and 1.7 for arch and gravity dam, respectively).

Figure 2a show the sensitivity analysis of the K coefficient for a Turbulence index $T_u = 0.013$ (gravity dam). We can observe that for $K = 1$ the break-up length is very similar to the arch dam case ($T_u = 0.012$ and $K = 0.85$). Since in this case the turbulence index is somewhat greater than in the arch dam, then it seems reasonable that the length of disintegration is less. In this way was established $K = 0.95$. Figure 2b confirms that in the gravity dam case the initial conditions corresponding to $T_u = 0.013$ and $K = 0.95$.
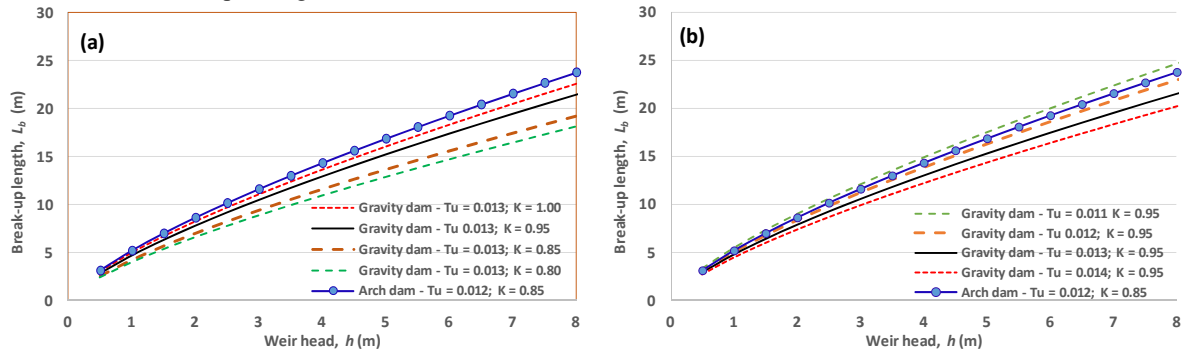
Figure 2. Break-up length in function of weir head for arch and gravity dam (Castillo and Carrillo 2016a).

Figure 3 show the sensitivity analysis for K_φ parameter in function of relation H / h and $T_u = 0.013$. We can conclude that the jet expansion term for a gravity dam ($T_u = 0.013$ and $K_\varphi = 1.14$) is equal to the arch dam case (($T_u = 0.012$ and $K_\varphi = 1.24$). However, the jet expansion term should be slightly higher for the gravity dam case so it was established that $K_\varphi = 1.20$ (intermediate value between a circular jet, $K_\varphi = 1.14$ and a nappe flow case, $K_\varphi = 1.24$).
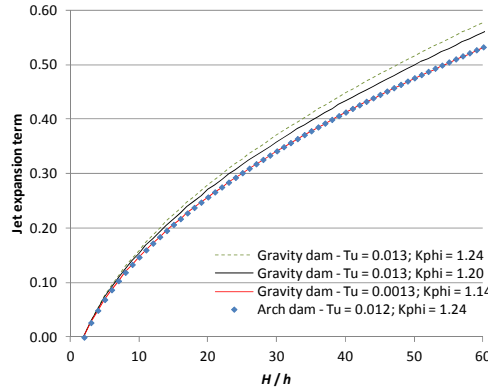
Figure 3. Jet expansion in function of the H/h relation and the K_φ parameter (Castillo and Carrillo 2016a).

During the falling, the energy dissipation is due to the air entrainment into the falling jet and the depth of water upstream of the jet. In Figure 4, the velocity V_j and the jet thickness B_j at the impingement conditions, the core depth or minimum depth for effective water cushion and the two principal eddies that produce the dominant frequencies in the plunge pool (large scale eddies and shear layer structures) are sketched. The lowest frequencies correspond to large scale eddies that have a dimension on the order of the plunge pool depth. Then, the recirculation velocity for large plunge pools is about $V_r \sim 0.035\, V_j$ and the corresponding Strouhal number of the dominant eddies is $S = fY/V_j = (V_r/\pi Y)\,(Y/V_j) \sim 0.01$ (Ervine and Falvey 1987; Ervine et al. 1997). The following dominant frequency corresponds

to eddy sizes contained in half of the shear-layer width and is proportional to the entry jet velocity; then, the Strouhal number of the shear-layer eddies is equal to a constant $S_s = (f_s Y/V_j) = K_3 \sim 0.25$, and it coincides with the spread of the jet into the water cushion as shown on Figure 4 (Ervine and Falvey 1987; Ervine et al. 1997).

Energy dissipation in the basin by diffusion effects can only be produced if there is an effective water cushion ($Y/B_j > 5.5$ for the nappe flow case, Castillo et al. 2015). The instantaneous pressures signals obtained on the bottom of the plunge pools may be adjusted in curves for different ranges (see Figure 5).
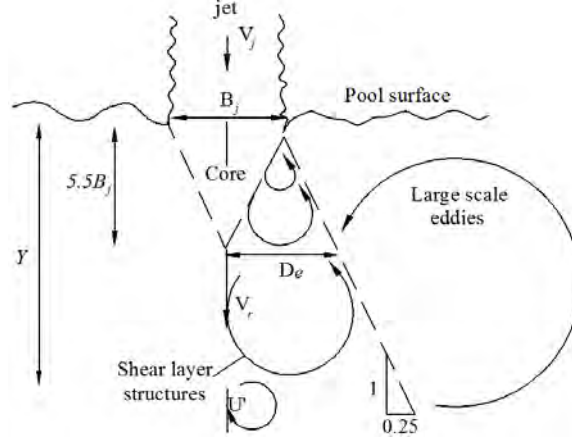
Figure 4. Eddy structures in effective water cushion ($Y \geq 5.5 B_j$): large scale eddies size ~Y and shear layer structures size ~De (adapted from Ervine et al. 1997).

The dynamic pressures are a function of the fall height to disintegration height ratio, H/L_b, and water cushion to impingement jet thickness ratio, Y/B_j (Figure 5a). The dynamic pressure on the bottom of the stilling basin is based on two components: the mean dynamic pressure, C_p, (Figure 5b) and the fluctuating dynamic pressure, C_p', (Figure 5c). These dynamic pressure coefficients are used as estimators of the stream power reduction coefficients, by an effect of the jet disintegration in the air and their diffusion in the stilling basin. Thus, the total dynamic pressure is expressed as:

$$P_{total} = C_p(Y/B_j)P_{jet} + FC_p{'}(Y/B_j)P_{jet}$$

(2)

where $C_p(Y/B_j)$ is the mean dynamic pressure coefficient; $C_p'(Y/B_j)$ the fluctuating dynamic pressure coefficient; P_{jet} the stream power per unit of area, and F the reduction factor of the fluctuating dynamic pressure coefficient (for rectangular jet or nappe flow case, $F = 1$). In nappe flow case, Carrillo (2014) and Castillo et al. (2015, 2017) adjusted the formulae by using new laboratory data (Figure 5).

- Mean dynamic pressure coefficient (C_p)

If $Y / B_j \leq 5$ and $H / L_b < 0.85$:

$$C_p = 1 - 0.0037e^{5.2484(H/L_b)}$$

(3a)

If $H/L_b \geq 0.85$:

$$C_p = 0.456(H/L_b)^{-2.393}$$

(3b)

If $Y / B_j > 5$:

$$C_p = \frac{H_m - Y}{V_j^2/2g} = ae^{-b(Y/B_j)}$$

(3c)

where H_m is the head mean registered at plunge pool bottom (stagnation point) and V_j the mean velocity in impingement conditions. In Table 1 are presented the parameters a and b, the regression coefficient R^2 and the mean dynamic pressure coefficient C_p, when the ratio $Y/B_j < 5.5$.

Table 1. Parameters *a* and *b* of the mean dynamic pressure coefficient when $Y > 5.5B_j$ and C_p values when $Y < 5.5B_j$.

H/L_b	a	b	R^2	C_p ($Y/B_j < 5.5$)
< 0.75	1.740	- 0.155	0.893	0.802
0.75-0.85	1.850	- 0.180	0.921	0.752
0.85-1.05	1.550	- 0.175	0.868	0.646
1.05-1.15	1.200	- 0.160	0.822	0.539
1.15-1.25	1.200	- 0.175	0.836	0.500
1.25-1.35	1.130	- 0.185	0.731	0.448
1.35-1.60	0.390	- 0.190	0.749	0.151
≥ 1.60	0.160	- 0.135	0.722	0.081

- Fluctuating dynamic pressure (C'_p)

$$C'_p = \frac{H'}{v_j^2/2g} \tag{4a}$$

where H' is the root mean square of instantaneous pressures. The best fit obtained to quantify the fluctuating dynamic pressure coefficient as a function of the ratios Y/B_j and H/L_b is obtained with two fit types:

For $Y/B_j < 14$, polynomial fit:

$$C'_p = a\left(\frac{Y}{B_j}\right)^3 + b\left(\frac{Y}{B_j}\right)^2 + c\left(\frac{Y}{B_j}\right) + d \tag{4b}$$

For $Y/B_j \geq 14$, potential fit:

$$C'_p = a\left(\frac{Y}{B_j}\right)^b \tag{4c}$$

The different coefficients and relations between H/L_b and Y/B_j are presented in Table 2.

Table 2. Coefficient values for calculating the fluctuant dynamic pressure coefficient.

H/L_b	$0 \leq Y/Bj < 1$				$Y/Bj \geq 14$		R^2
	a	b	c	d	a	b	
≤ 0.75	0.0003000	-0.0086	0.0590	0.100	0.300	0.120	0.72
0.75-0.85	0.0003400	-0.0090	0.0500	0.200	0.400	0.130	0.76
0.85-1.05	0.0003450	-0.0100	0.0625	0.230	0.600	0.140	0.66
1.05-1.35	0.0000005	-0.0017	0.0130	0.240	0.700	0.140	0.70
1.35-1.60	0.0003000	-0.0017	0.0070	0.210	1.500	0.150	0.81
>1.60	0.0002000	-0.0054	0.0290	0.140	1.050	0.240	0.75
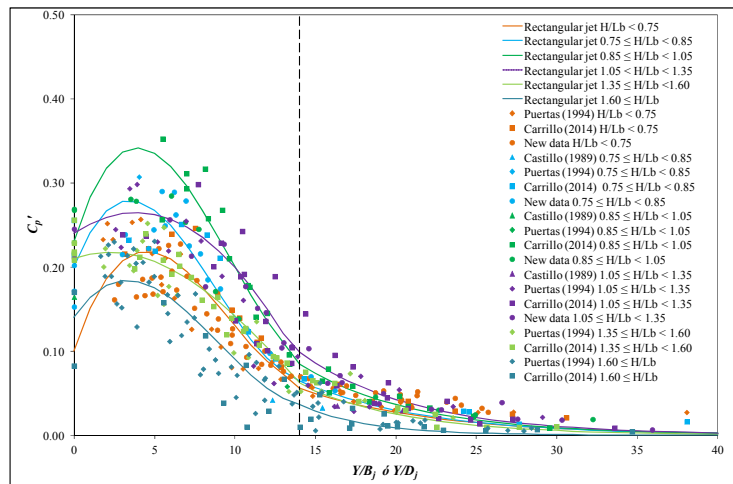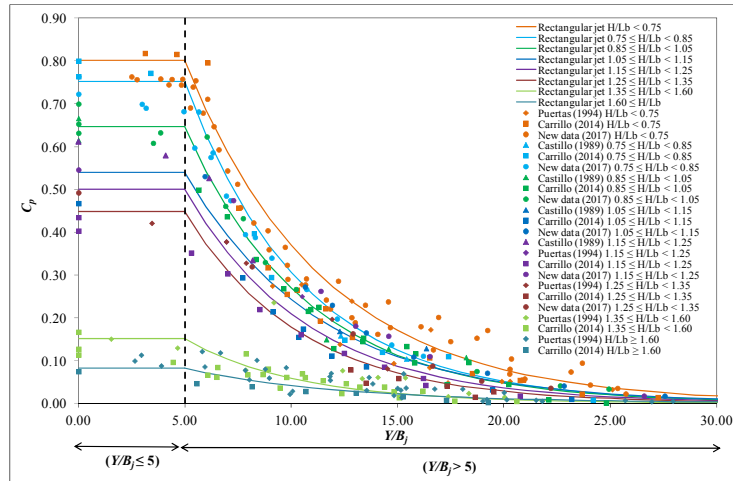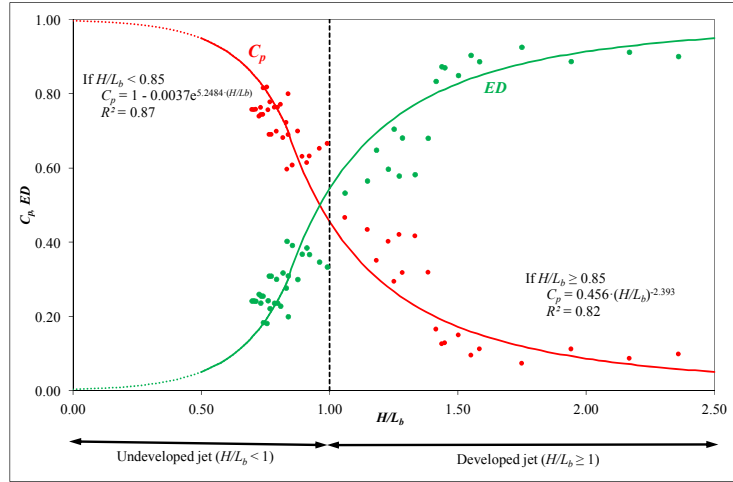
Figure 5. Pressure coefficients for the rectangular jet or nappe flow case: (a) Mean dynamic pressure coefficient and energy dissipation in the air in function of H/L_b ($Y/B_j \leq 5.5$). (b) Mean dynamic pressure coefficient, C_p. (c) Fluctuating dynamic pressure coefficient, C_p'.

In order to know the pressure distribution around of the stagnation point, the following formula was considered (Figure 6):

$$\frac{P}{H_m} = e^{-\emptyset(x/b_{distrib})} \tag{5}$$

where ϕ is an adjustment parameter and $b_{distrib}$ is the width of the pressure influence region (distance between the upstream and downstream points where $p = H_m/2$).

The developed jets ($H/L_b>1$) have a greater pressure distribution region than undeveloped jets ($H/L_b \leq 1$). Aki (1969) formula ($b_{distib} = 0.13Y$) is more extended than the envelope of the mean dynamic pressures proposed by the other authors. The Cola (1966), Aki ($b_{distib} = 0.23Y$ proposed by Xu Duo-Ming and Yu Chang-Zhao 1983), Hartung and Häusler (1973) when $y_k = 7.2B_j$ and Beltaos (1976) formulae were obtained for a non-aerated jets. Their results are in agreement with the lower envelope of the data obtained in the laboratory (with a smaller aeration). The Hartung and Häusler distribution (when $y_k = 5B_j$) shows results between those proposed by the other authors. Through using the same general expression different upper envelopes have been obtained. For $H/L_b \leq 1$, a parameter $\phi = 10$ has been obtained. For $H/L_b > 1$, the jets are very aerated and the influence region greater, obtaining a parameter $\phi = 7$.
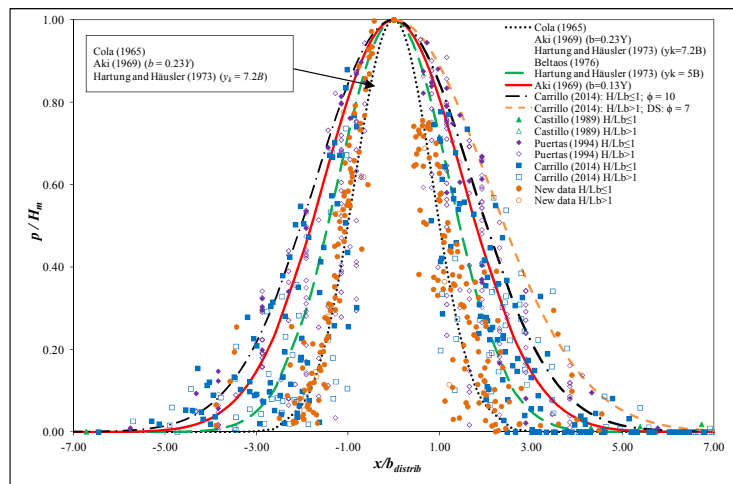
Figure 6. Pressure distribution near the stagnation point of the plunge pool as a function of $b_{distrib}$: width of the pressure influence region (distance between the upstream and downstream points in which $p = H_m / 2$).

Within the plunge pool downstream of the impingement point, the flow resembles in a submerged hydraulic jump and a wall jet. However, the situation is complicated here by the air entrainment. Several formulas have been put forward to express the horizontal velocity distribution in the vertical direction. We return to some of these formulas later in the paper. In Castillo et al. (2014), the so-called "homogeneous" theoretical model of CFX was employed. It was shown that this model is able to reproduce correctly the jet water velocity, and the averaged pressures in the plunge pool. There is always a challenge in modeling two-phase flows to discern which level of complexity is needed to represent different aspects of the flow (Bombardelli and Jha 2009). One of the objectives of this paper was to determine whether this theoretical model is sophisticated enough to represent velocities in the plunge pool. New laboratory data were obtained and new three-dimensional simulations were carried out. ANSYS CFX was again selected due to the variety of turbulence closures available in the code, the previous experience with it and, more importantly, due to the diverse two-phase flow models embedded in the package, which can allow us to expand the research further in the long-term future.

2. EXPERIMENTAL FACILITY

2.1. Turbulent jet experimental facility

The experimental facility was constructed at the Hydraulics Laboratory of the Universidad Politécnica de Cartagena, and was described in detail in Carrillo and Castillo (2014). The facility consists of a mobile mechanism which permits to vary the weir height between 1.7 and 3.5 m, and flows from 10 to 150 l/s. It has an inlet channel with a length of 4.0 m and width of 0.95 m. The discharge is produced through a sharp-crested weir with a width of 0.85 m and height of 0.37 m. The plunge pool, in which different water cushions may be simulated, is a 1.3-m high, 1.1-m wide and 3.0-m long methacrylate box. Turbulent kinetic energy values at the inlet channel were obtained with an Acoustic Doppler Velocimeter (ADV); mean velocities and air concentrations in different sections of the falling jet were acquired with optical fiber instrumentation; and instantaneous pressure values were measured with piezoresistive transducers located on the basin bottom. In addition, ADV and optical fiber were used in the basin to obtain velocity and air concentration profiles, respectively, downstream of the impingement point. Figure 7a shows a picture of the experimental device in which sizable values of air concentration are apparent.

2.2. Optical fiber equipment

To measure the air concentration at the falling jet and at the basin, an RBI-instrumentation dual-tip probe optical fiber phase-detection instrument was used. This equipment enables measurement in water up to 20 m/s flow velocity and the relative uncertainty concerning the void fraction is estimated at about 15% of the measured value (Stutz and Reboud 1997). The rise and fall of the probe signal corresponds, respectively, to the arrival and the departure of the gas phase at the tip of the sensor. The void fraction was defined as the ratio of the total time the probe is in gas (Σt_{Gi}) to the experiment duration time t. Figure 7b shows the air concentration in different sections downstream of the jet stagnation point. The maximum air concentration is around 12% (at a distance of 21% from the bottom) for the first sections. However, from the section 0.30 m and a distance from the bottom smaller than 70%, the air concentration is below 10%. Concentrations remain high still at the upper portion of the water depth in the basin.
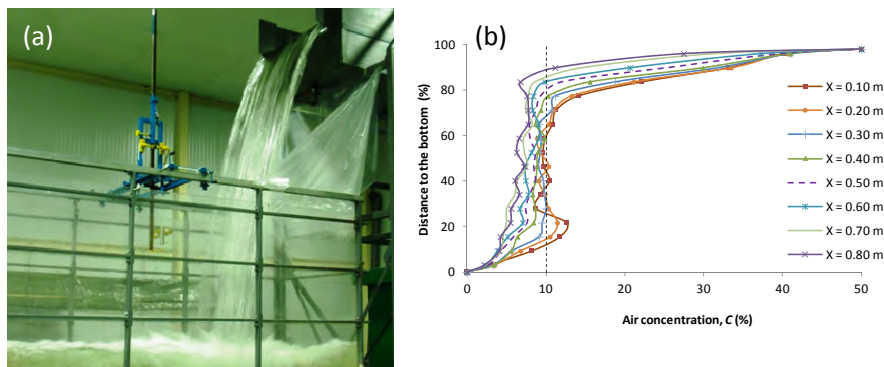
Figure 7. (a) Device of turbulent jets. (b) Air concentration in the basin for different sections downstream of the jet stagnation point. Measurements obtained by means of an optical fiber ($q = 0.082$ m²/s, $H = 2.19$ m, and $Y = 0.32$ m) (Castillo and Carrillo 2016a).

2.3. Acoustic Doppler Velocimeter (ADV)

In order to characterize the macro turbulence of the flow in the plunge pool, 5000 values were recorded in each measured point by using a frequency of 10 Hz (more than eight minutes of observation). In this way, 2006 points in the symmetrical vertical plane of the basin were obtained. As the flows are highly turbulent, the values obtained with ADV may be affected by spurious signals or "spikes". Furthermore, in this particular case, the air may also affect the signal of the ADV. Frizell (2000) experimented with the air effect, measuring concentrations varying from

0 – 3.61%. As the air concentrations increase and bubble sizes increase, correlation values drop dramatically as the acoustic signals used by the probe are absorbed and reflected by the two-phase flow mixture. Matos et al. (2002) also found that air bubbles affect the accuracy of velocity measurements taken with the ADV. However, their experimental results suggest that the ADV can provide reasonable estimates of the velocity for low air concentrations up to 8%.

2.4. Large Scale-Particle Image Velocimetry

Large-Scale Particle Image Velocimetry (LS-PIV) is an extension of particle image velocimetry (PIV), which provides velocity fields spanning large flow areas in laboratory or field conditions. Additional data, such as mappings of large-scale flow structures and discharges are readily obtainable using LS-PIV. While the images and data-processing algorithms are similar to the conventional PIV technique, adjustments are required for illumination, seeding procedures, and pre-processing of the recorded images (Fujita et al. 1998). This technique has been used to estimate the velocity of free falling jets (Bercovitz et al. 2016).

In present work, the flow was recorded with a high-speed camera FASTCAM SA3 Model 120K (Photron Limited), a zoom lens with 50 mm focal length by Nikkor, lens aperture f/5.6, 1024x1024 pixels resolution, 8 bits→255 shades and a horizontal distance from the camera to the jet recorded of around 3.50 m. Hence, the recording window dimensions were around 0.9 m x 0.9 m. Illumination of experiment was reached with 8 regular 800 w light bulbs with reflecting mounts in front of the flow. The speed camera used was 500 Hz; 0.00105 (m/pixel). Frames were analyzed in consecutive pairs by cross-correlation algorithm in an interrogation area of 64 x 64 pixels with sub-windows of 32 x 32 pixels in a single pass search and overlapping of 50% (Adrian and Westerweel 2010). No background slide subtraction or noise remove techniques were applied. The PIVlab 1.41 software was used for the cross-correlation. This program is an open-source time-resolved particle image velocimetry tool in MATLAB® (Thielicke and Stamhuis 2014). In each test, 1360 images were recorded and each test was repeated four times. The velocity values were averaged at each sub-window. Figure 8 shows the velocity field obtained with a pair of images.

Distances in the recorded window were calibrated considering a vertical plane located at the toe of the jet, at 3.30 m of horizontal distance to the camera. These distances were projected over the upper nappe profile to achieve the real displacements of the flow, with ratios from 1/1.15 in the upper zone, to 1/1.00 in the lower part of the recorded window. To do this, it was assumed that the shape of the upper nappe profile agrees with that proposed by Scimemi (1930) at each sub-window. The agreement between the lab measurements and the Scimemi (1930) formula was verified by Carrillo (2014). Figure 8c shows the sub-window length obtained from the projection of each segment in the vertical plane used to calibrate the distance.
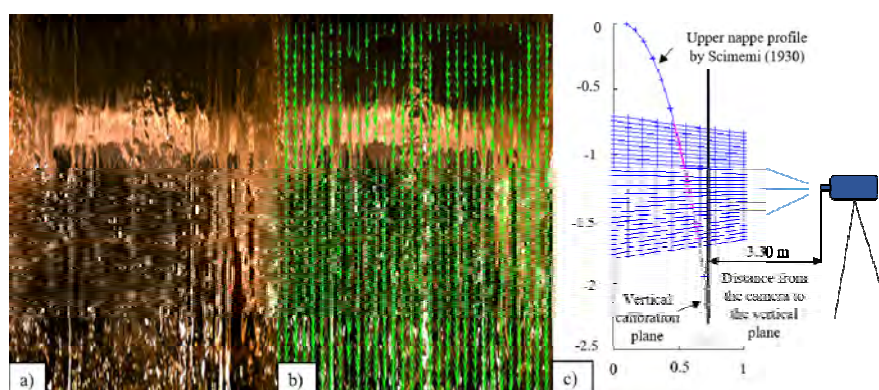
Figure 8. a) Image recorded with 500 Hz frequency; b) Velocity field defined by Cross Correlation PIV technique between a pair of images; c) Scheme of the projection of the vertical segments over the upper nappe profile proposed by Scimemi (1930)(Carrillo et al. 2018).

3. MATHEMATICAL AND NUMERICAL MODELING

As can be seen from Figure 7, the flow conditions in the plunge pool are such that the air concentrations are relatively elevated at the point of jet impingement and nearby areas and in the top layer of the water depth. In these areas, there is a mostly non-dilute, two-phase flow. However, as we move far from the impingement point, the flow conditions tend to become quasi-dilute. That is why we decided to solve the equations for the conservation of mass and momentum for the mixture, which may be written in compact form (ANSYS CFX Manual 2015) as:

$$\frac{\partial(\rho\phi)}{\partial t} + \frac{\partial}{\partial x_j}\left[\rho U_j \phi - \Gamma \frac{\partial \phi}{\partial x_j}\right] = S \tag{6}$$

where ϕ is the transported quantity, i and j are indices which range from 1 to 3, x_i represents the coordinate directions (1 to 3 for x, y, z directions, respectively), and, t the time. In turn, $\rho = \sum_{k=1}^{Np} r_k \rho_k$, $U_j = \frac{1}{\rho}\sum_{k=1}^{Np} r_k \rho_k U_{kj}$, and $\Gamma = \sum_{k=1}^{Np} r_k \Gamma_k$, with r_k indicating the volume fraction of k-th fluid, Γ_k denoting the diffusion coefficient associated with the transported quantity for phase k, N_p denoting the number of phases and S indicating the sources/sinks for the transported quantity (ANSYS CFX Manual 2015). In this model, phases share the same velocity field. When $\phi = 1$, $S = 0$, and $\Gamma = 0$, the mass conservation equation is recovered, and when $\phi = U_i$, the momentum equation is recovered, with its corresponding source terms to account for the Reynolds stresses.

The theoretical model comes as a result of the addition of the equations of the two phases (Drew and Passman 1999; ANSYS CFX Manual 2015). Further, $\phi_K = \phi$. Rigorously speaking, models like this have been found to provide adequate predictions only in relatively-dilute mixtures. For larger concentrations they found that the velocity distribution could not be well predicted relatively far from the wall with mixture models. Thus, we expect the "homogeneous" model to be able to represent rather adequately those areas in which air concentrations are not that high. As said, the code ANSYS CFX has been used, which is based on an element-oriented, finite-volume method (FVM). It allows different types of volumes, including tetrahedral and hexahedral volumes. Solution variables are stored at the nodes (mesh vertices). More details are given in the ANSYS CFX Manual (2015).

3.1. Turbulence models

In this work, one of the most usual two-equation turbulence models have been tested for the free falling jet and basin case. Two-equation models use the gradient diffusion hypothesis to relate the Reynolds stresses to the mean velocity gradients and the turbulent viscosity. The eddy viscosity hypothesis considers that eddies behave like molecules and the Boussinesq model assumes that the Reynolds stresses are proportional to the mean velocity gradients, as follows (Pope 2000):

$$-\rho\overline{u_i' u_j'} = \mu_t \left(\frac{\partial U_i}{\partial x_j} + \frac{\partial U_j}{\partial x_i}\right) - \frac{2}{3}\delta_{ij}(\rho k) \tag{7}$$

with μ_t being the eddy viscosity or turbulent viscosity, $k = 1/2(\overline{u_i' u_i'})$ is the turbulent kinetic energy and δ_{ij} the Kronecker delta. The k-ω based Shear-Stress Transport (SST) model (Menter 1994) assumes that the eddy viscosity is linked to the turbulence kinetic energy, k, and the turbulent frequency, ω, as $\mu_t = \rho\frac{k}{\omega}$. The SST model takes into account the accuracy of the k-ω model in the near-wall region and the free stream independence of the k-ε model in the outer part of the boundary layer. It is considered as a hybrid model (see Rodi et al. 2012).

3.2. Free surface modeling

The Free Surface model assumes that each control volume contains three possible conditions:
- $r_k = 0$ if cell is empty (of the k-th fluid);
- $r_k = 1$ if cell is full (of the k-th fluid);
- $0 < r_k < 1$ if cell contains the interface between the fluids.

Tracking of the interface between fluids is accomplished by the solution of the volume fraction equation.

4. MODEL IMPLEMENTATION IN THREE DIMENSIONS

The model boundary conditions corresponded to the turbulence kinetic energy at the inlet obtained with ADV (located 0.50 m upstream of the weir), the upstream and downstream water levels and their hydrostatic pressure distributions. ANSYS CFX has different treatments near the wall. ω-based turbulence models (e.g. SST) use automatic wall functions which switch between regular wall functions (Pope 2000) and low-Reynolds wall treatment (Menter 1994). Considering the wall treatment used by ANSYS CFX, the mesh sizes close to the solid boundary were smaller than in the rest of the domain. Values of $y^+ = yu^*/\nu$, were smaller than 40 (y is the flow depth, u^* the wall friction and ν the water kinematic viscosity). The symmetry condition in the longitudinal plane of the plunge pool was used.

The inlet condition considers the volumetric flow rate with a normal direction to the boundary ($q = 0.082$ m^2/s, $q = 0.058$ m^2/s, $q = 0.037$ m^2/s, $q = 0.023$ m^2/s) and the water level height at the upstream deposit (2.313 m for $q = 0.082$ m^2/s, 2.285 m for $q = 0.058$ m^2/s, 2.263 m for $q = 0.037$ m^2/s, 2.237 m for $q = 0.023$ m^2/s). The outlet condition was considered with flow normal to the boundary and hydrostatic pressure. The water level height at the outlet was modified according to the water cushion depth, Y, in the laboratory device. For all walls of the upper deposit, the weir and the dissipation basin, no slip smooth wall conditions were considered. The roughness of methacrylate was indicated in the walls. In the transverse direction, wall boundary conditions were used. Figure 9 shows the computational domain employed.
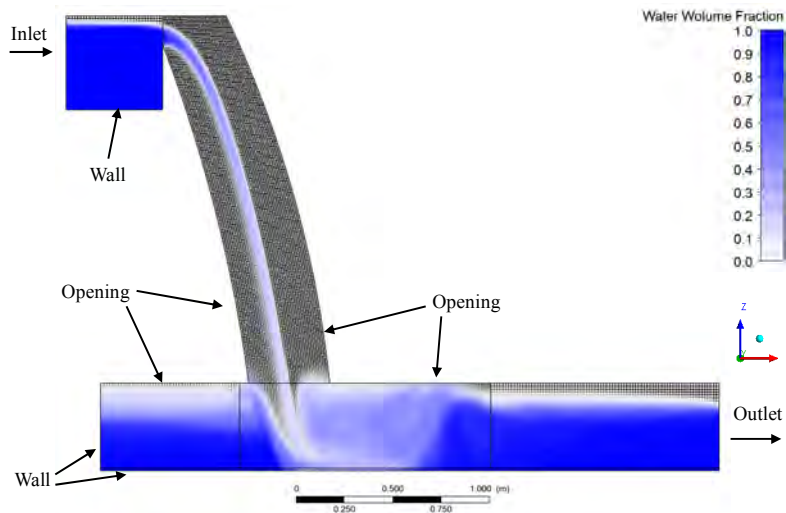
Figure 9. Schematic of computational domain and boundary conditions, mesh blocks and water volume fraction (Castillo et al. 2017)

4.1. Mesh-independence tests

In Figure 10a, the simulations result for the different mesh sizes (5, 7.5, 10, 12.5 and 15 mm) in the free falling jet, obtained as a function of the vertical distance to the weir in terms of the flow velocities in the jet, are shown. Differences in velocities with the optical fiber measurement are smaller than 2% in all the cases (Castillo et al. 2014). From the analysis of Figure 10b, it can be concluded that mesh-independence is reached with an element size of 10 mm. The results are in agreement with previous results obtained on pressures at the stagnation point (Castillo et al. 2014). In this way, the mesh size of 10 mm seems to be valid for the flow rates analyzed.
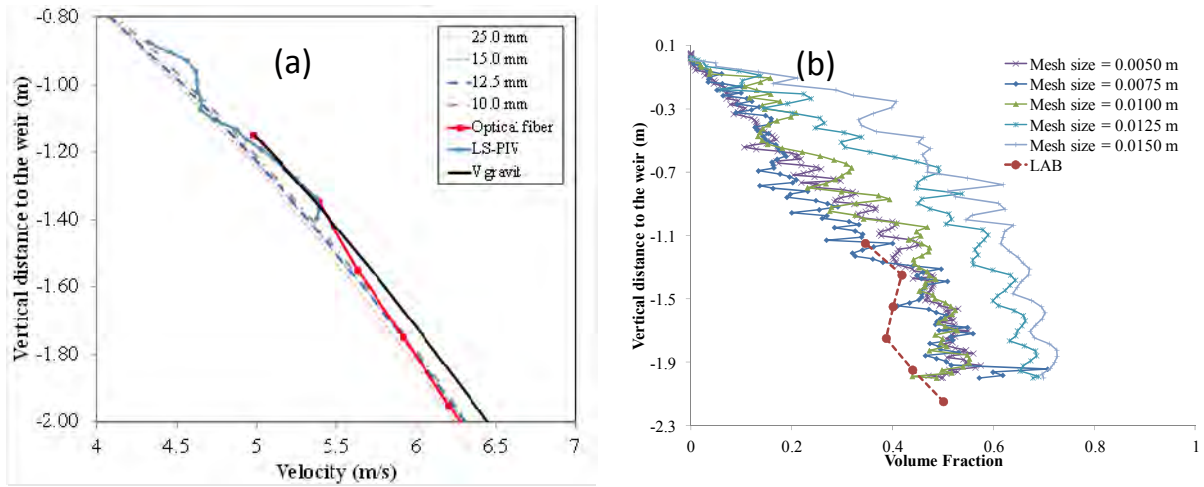
Figure 10. (a) Velocities and (b) Volume fractions as a function of the mesh size; $q = 0.058$ m^2/s, $h = 0.095$ m (Carrillo et al. 2018, Castillo and Carrillo 2016a).

4.2. Convergence criteria

To judge the convergence of iterations in the numerical solution, we monitored the residuals. The solution is said to have converged in the iterations if the scaled residuals are smaller than fixed values ranging between 10^{-3} and 10^{-6}. In this work, the residual values were set to 10^{-4} for all the variables. With this choice and for 791,354 elements (255,776 in the falling jet), the mean computational time was 7.2×10^5 seconds (≈ 8.3 days), using a Central Processing Unit (CPU) with sixteen processors (Intel® Xeon® E5-2699 v3 @ 2.30 GHz).

5. RESULTS AND DISCUSSIONS

5.1. Velocity and turbulent kinetic energy distribution in the plunge pool

We can compare the velocity profiles in the forward flow if they are normalized with a velocity scale equal to the maximum velocity, V_{max}, at any section, and with a length scale δ_l equal to the elevation y from the bottom where the local velocity $V = V_{max} / 2$, and the velocity gradient is negative (see Figure 11).
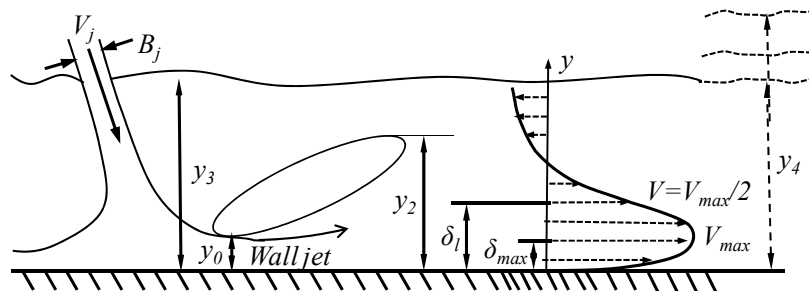
Figure 11. Velocity distribution sketch for submerged jumps (adapted from Wu and Rajaratnam 1996).

Velocities at different cross sections of the plunge pool located downstream of the stagnation point were measured with ADV. Results for the same cross sections were obtained from the CFD simulations (Castillo and Carrillo 2016a, Castillo et al. 2017). The velocities have been made dimensionless by using the maximum horizontal velocities in each cross section, $V_{max,x}$ (Figure 12a). In addition to the mean velocities, the turbulent kinetic energy profiles were also compared (Figure 12b). In general, the results from the numerical simulations show the same

behavior as the results obtained in the laboratory. Differences are important close to the stagnation point, where the numerical model may not obtain accurate results due to the relatively important air entrainment into the plunge pool (Figures 7a and 7b).
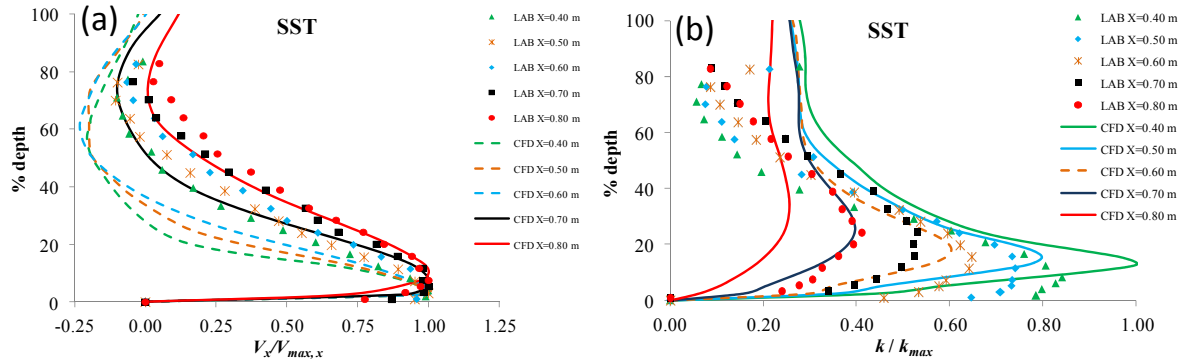
Figure 12. (a) Horizontal velocity profiles in the plunge pool downstream of the stagnation point.
(b) Turbulent kinetic energy profiles. SST model ($q = 0.082$ m^2/s, $H = 1.993$ m, $Y = 0.32$ m)
(Castillo and Carrillo 2016a).

Following Wu and Rajaratnam (1996), Figure 13a shows the results of the characteristic length obtained through the plunge pool. For each horizontal velocity profile measured with the ADV, the length scale δ_l was obtained in each section. Data have been classified as a function of the ratio water depth in the plunge pool/impingement jet thickness of each test. For ratios Y/B_j up to 20, the behavior is similar to that found in wall jets.

The values for water cushion depths Y/B_j up to 30 tend to fall within one standard deviation of the mean value. However, for larger water cushion depths, the characteristic length is higher. In this type of submerged hydraulic jump where the falling jet enters almost vertical, an equation may be obtained with the data that fall within one standard deviation of the mean value:

$$\frac{\delta_l}{B_j} = 0.465 \frac{X}{B_j} + 2.415 \qquad (8)$$
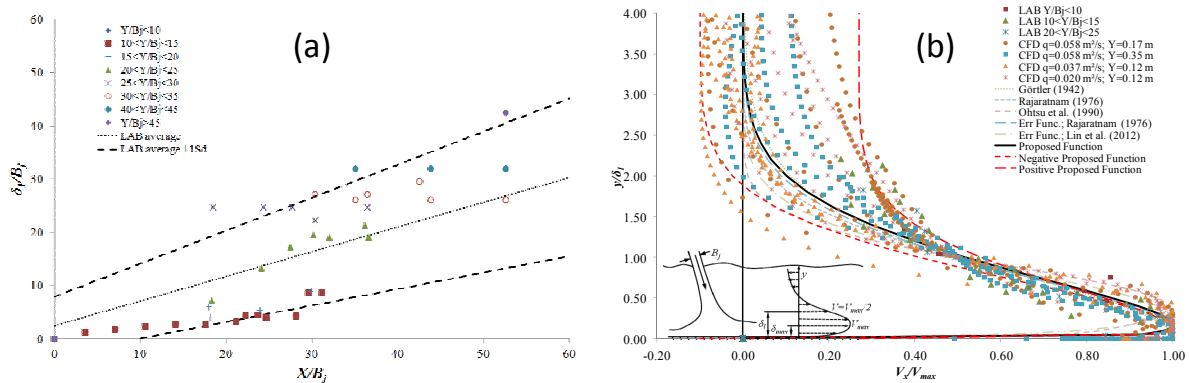
Figure 13. (a) Characteristic length δ_l in submerged hydraulic jumps. (b) Non-dimensional profiles of the horizontal velocity in the central vertical plane of the plunge pool (Castillo and Carrillo 2016a).

Figure 13b shows the velocity profiles obtained from the numerical simulations as well as the laboratory measurements in the laboratory, together with equations proposed by diverse authors for horizontal wall jets (Castillo and Carrillo 2016a). The overall behavior of the observations can be predicted rather well by existing equations up to $y/\delta_1 \approx 1.5$. Disagreements appear when ratio $V_x/V_{max} < 0.4$. This seems to be related to the angle of impingement of the jet. In hydraulic jump studies, the wall jet is horizontal, while the impingement free falling jet enters almost vertical. The higher scatter occurs when the water cushion depth is $Y/B_j > 20$. In this way, the self-similarity disappears when the velocity profiles are close to the stagnation point and when a very submerged condition is obtained for the hydraulic jump. With all data, a new regression is proposed for submerged hydraulic

jumps downstream of the impingement point:

$$\frac{V_x}{V_{max}} = 1.48 \left(\frac{y}{\delta_l}\right)^{1/7} \left(1 - erf\left(0.66\frac{y}{\delta_l}\right)\right) \tag{9a}$$

This proposed function is the separation line between the profiles in which there is negative recirculation flow and the profiles in which the flow is moving towards downstream.

For the range of flows and water cushions analyzed, the limit between both behaviors seems to be located at 0.2-0.3 m downstream of the stagnation point.

$$\frac{V_x}{V_{max}} = 1.65 \left(\frac{y}{\delta_l}\right)^{1/7} \left(1 - erf\left(0.72\frac{y}{\delta_l}\right)\right) - 0.10 \tag{9b}$$

$$\frac{V_x}{V_{max}} = 1.10 \left(\frac{y}{\delta_l}\right)^{1/7} \left(1 - erf\left(0.80\frac{y}{\delta_l}\right)\right) + 0.27 \tag{9c}$$

5.2. Energy dissipation in the plunge pool

In a horizontal channel, the total energy variation between the sections located upstream and downstream of the submerged hydraulic jump are, by definition:

$$H_L = \left(\frac{V_j^2}{2g} + y_3\right) - \left(\frac{V_4^2}{2g} + y_4\right) \tag{10a}$$

where y_3 and y_4 are the water depths upstream and downstream of the submerged hydraulic jump generated by the jet. By using Eq. (10a) with the continuity equation, the energy dissipation may be obtained as (Othsu et al. 1990)

$$\frac{H_L}{H_0} = \frac{2\left(\frac{y_3}{y_0} - \frac{y_4}{y_0}\right) + \left(1 - \frac{1}{(y_4/y_0)^2}\right)F_{r0}^2}{2(y_3/y_0) + F_{r0}^2} \tag{10b}$$

where H_0 is the energy upstream of the hydraulic jump, and y_0 and F_{r0} the water depth and Froude number in the upstream section of the hydraulic jump. When $y_3 = y_0$ and $y_4 = y_2$, the free hydraulic jump expression is recovered.

Figure 14a shows the contrast between the relative energy dissipation and the Froude number at the jet impingement condition, $F_j = V_j/\sqrt{gB_j}$, obtained from experiments. In addition, results coming from the use of Eq. (14b) have been included as a function of the ratio between the upstream water depth and the impingement jet thickness (y_3/B_j). In the laboratory device, the impingement Froude number is between 13 and 20 for the impingement jet thickness of 0.015 m plotted in Figure 14b. In general, tests carried out show an energy dissipation larger than 75% of the impingement jet energy. This ratio increases when the ratio y_3/B_j decreases (Castillo et al. 2016).
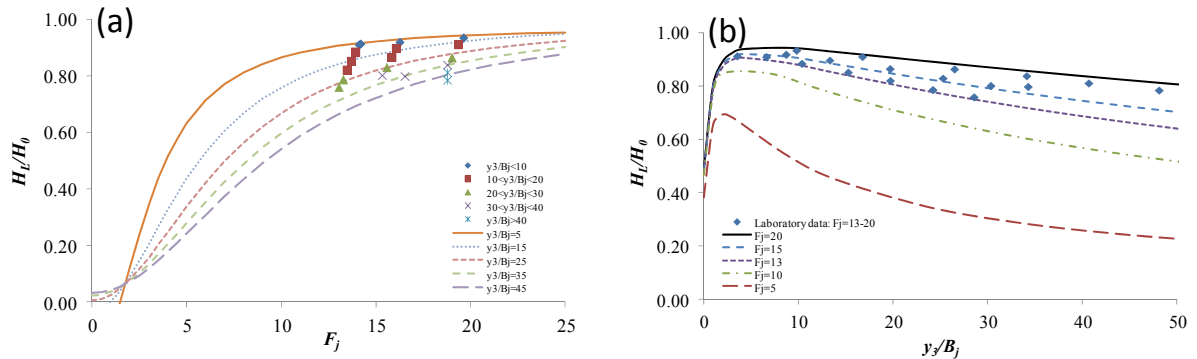
Figure 14. Relative energy dissipation in the plunge pool: (a) in function of the impingement Froude number. (b) in function of the ratio y_3/B_j for the cases $B_j = 0.015$ m and $F_j = 13$ - 20 (Castillo and Carrillo 2016a).

6. STUDY CASES

6.1. Paute - Cardenillo Dam

The Paute-Cardenillo Dam, located in Ecuador, is a double curvature arch dam with a maximum height of 135 m to the foundations (Figure 15a). The top level is 926 meters above mean sea level (MASL), while the normal maximum water level is 924 MASL. The river bed consists of a layer of 24 m of alluvial, below which there is a layer of 10 m of weathered rock (Figure 15b). Table 3 shows the particles characteristics size of the alluvial (24 m) and the weathered rock (10 m) in the Paute River.
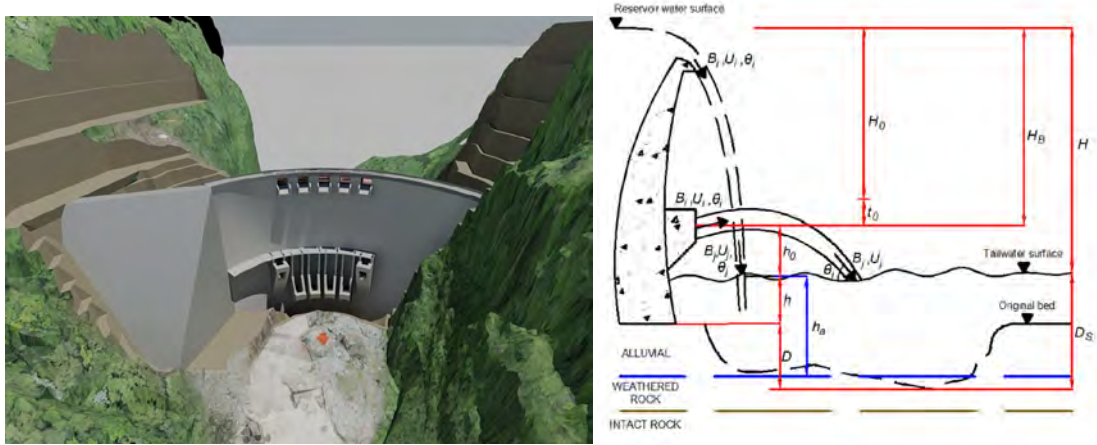
Figure 15. Paute-Cardenillo Dam (**a**) Three-dimensional view;
(**b**) Scheme of scour (Castillo and Carrillo 2016b).

Table 3. Particles characteristic size of the bed material.

Bed material	D_{16} (m)	D_{50} (m)	D_{84} (m)	D_{90} (m)	D_m (m)
Alluvial (820 MASL to 796 MASL)	0.006	0.150	0.225	0.240	0.124
Weathered rock (796 MASL to 786 MASL)	0.045	0.160	0.500	0.550	0.235

The dam has a free surface weir controlled by five folded gates (7.20 x 5.60 m) that spill a flow of $Q_4 = 700$ m^3/s (return period TR = 4 years) and a half-height outlet with two almost symmetrical ducts (5.00 x 5.80 m). Considering the maximum normal operating level (924 m), the intermediate outlet capacity is $Q_{40} = 1760$ m^3/s. Hence, the total flow of the weir and half-height outlet is $Q_{100} = 2340$ m^3/s. Bottom outlet consists of four radial gates (5.00 x 6.80 m). The total discharge capacity of the dam is $Q_{10000} = 5520$ m^3/s (Consorcio PCA [1]).

EMPIRICAL FORMULAE

In the study, we examined 29 formulae. We estimated the scour hole for flows of various return periods. Most of the equations were obtained by dimensional and statistic analysis of data obtained in Froude scale reduced models, with few formulae based on prototypes and many obtained for the ski-jump. As discharge is produced by a free surface weir and in pressure conditions by an intermediate outlet, we modified the general expression which provides the following simplified general expression:

$$D_s = h + D = \Gamma \frac{q^x H_n^y h^w}{g^v d^z} \tag{11}$$

where D_s is the scour depth below tailwater level, h the tailwater depth, D the scour depth below the original bed,

Γ an experimental coefficient, q the specific flow, H_n the energy net head, and d the characteristic size of bed material. The meaning of the rest variables can be seen in Figure 15b.

In Equation 11 and in Figure 15b, x, y, z, v and w are empirical exponents defined by regression or optimization, t_0 the energy loss in the duct, $H_n = H_0 = H_B - t_0$ the net energy head at the exit of the outlet, H the falling height from reservoir level to tailwater level (ski-jump and free surface weir), h_0 the vertical distance between the outlet exit and the tailwater level, h_a the vertical distance between the tailwater level and the scour bed, B_i, U_i, θ_i the thickness, velocity and angle of the jet in initial condition, B_j, U_j, θ_j the total thickness, velocity and angle of the jet in the impingement conditions.

Tables 4 and 5 show the coefficients corresponding to five simplified and general formulae whose scour values fall in the range of the mean value ± one standard deviation at each specific flow rate. The process was repeated twice.

Table 4. Coefficients of five scour simplified formulae.

Author	Γ	x	y	z	d
Hartung (1959)	1.400	0.64	0.360	0.32	d_{85}
Chee and Padiyar (1969)	2.126	0.67	0.180	0.063	d_m
Bisazand and Tschopp (1972)	2.760	0.50	0.250	1.00	d_{90}
Martins-A (1955)	1.500	0.60	0.100	0.00	-
Machado (1980)	1.350	0.50	0.3145	0.0645	d_{90}

Table 5. Five scour general formulae.

Author (year)	Formulae	Parameters
Jaeger (1939)	$D_s = 0.6 q^{1/2} H_n^{1/4} (h/d_m)^{1/3}$	d_m = average particle size of the bed material
Rubinstein (1963)	$D_s = h + 0.19 (\frac{H_n + h}{d_{90}})^{3/4} \left(\frac{q^{6/5}}{H_n^{23/49} h^{1/3}} \right)$	d_{90} = bed material size, 90% is smaller in weight
Mirskhulava (1967)	$D_s = (\frac{0.97}{d_{90}^{1/2}} - \frac{1.35}{H_n^{1/2}}) \frac{q \cdot \sin\theta_T}{1 - 0.175 \cdot \cot\theta_T} + 0.25h$	θ_T = impingement jet angle; g = gravity (9.81 m/s²); β = air-water relationship; ρ = water density
Mason (1989)	$D_s = 3.39 \frac{q^{3/5} (1+\beta)^{3/10} h^{4/25}}{g^{1/3} d^{3/50}}$	ρ_s = density of sediment; Γ = experimental coefficient
Bombardelli and Gioia (2006)	Axisymmetric jet: $D_s = \Gamma \frac{q^{2/5} H_n^{2/5}}{g^{1/5} d^{2/5}} \left[\frac{\rho}{\rho_s - \rho} \right]^{-3/5}$	

Figure 16 shows the results obtained for the free surface weir. We indicated the range of the mean value ± one standard deviation. The maximum scour that is possible to simulate is until the weathered rock depth (total scour 34 m) because the intact rock represents a rigid boundary condition in the empirical formulae of scour. Considering the mean value for the design flow (700 m³/s), the scour could reach a depth of 17 m. However, taking into account the mean value + 0.50 standard deviation, then the design flow fully penetrate the alluvial (scour 24 m). Considering the mean value + a standard deviation, the design flow could reach the intact rock layer (scour 34 m).

Figure 17 shows the results obtained for the half-height outlet. The range of the mean value ± one standard deviation and 0.50 standard deviation are indicated. For mean values the jet would scour the alluvial layer (24 m) with a return period flow $Q_{22} = 1320$ m³/s. The design flow ($Q_{40} = 1760$ m³/s) would penetrate over 32 m and not reach the intact rock. However, with the mean value + 0.50 standard deviation, the flow of 1550 m³/s would already erode completely the weathered rock layer (scour 34 m).
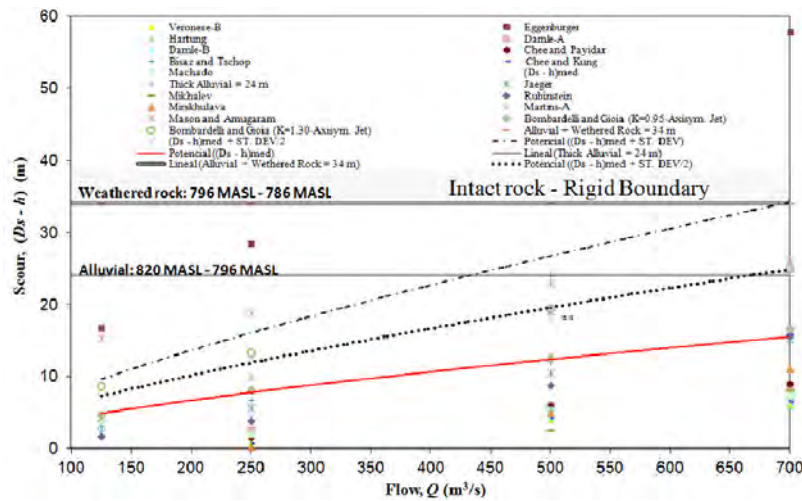
Figure 16. Scour of alluvial and weathered rock for the free surface weir (Castillo and Carrillo 2016b).
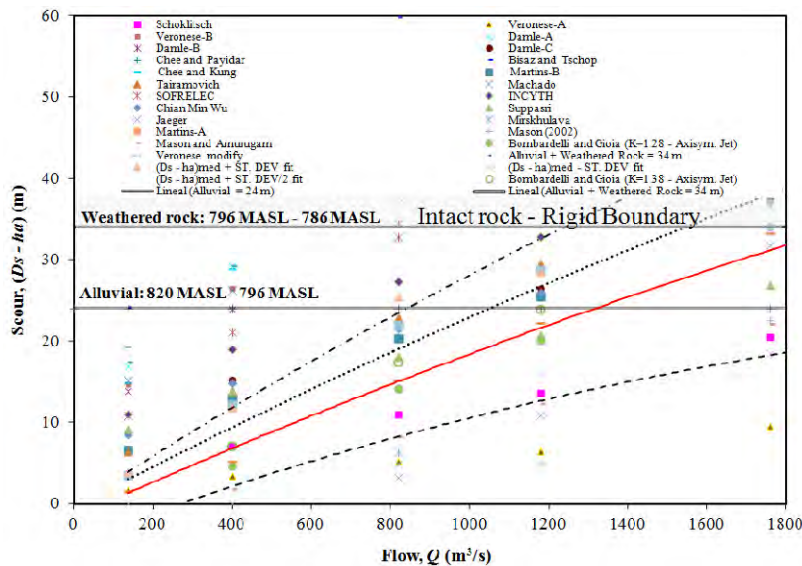
Figure 17. Scour of alluvial and weathered rock for the half-height outlet (Castillo and Carrillo 2016b).

SEMI-EMPIRICAL METHODOLOGY

The erodibility index is based on an erosive threshold that relates the magnitude of relative erosion capacity of water and the relative capacity of a material (natural or artificial) to resisting scour. There is a correlation between the stream power or magnitude of the erosive capacity of water (P) and a mathematical function [$f(K)$] that represents the relative capacity of the material to resist erosion (Annandale 1995).

Scour in turbulent flow is not a shear process. It is caused by turbulent and fluctuating pressures. Quantification of pressure fluctuations of incident jets in stilling basins has been studied mainly by Ervine and Falvey (1987), Ervine *et al.* (1997), Castillo (1989, 2006), Puertas (1994), Bollaert and Schleiss (2003), Manso (2006), Felderspiel (2011), Castillo *et al.* [2014, 2015], Carrillo (2014), Castillo and Carrillo (2014, 2015, 2016a, 2016b), Carrillo and Castillo (2014) and Castillo *et al.* (2014, 2015, 2017). Some of the main results of these papers have been included in FEMA (2014).

The dynamic pressures of jets are a function of the turbulence intensity at the discharge conditions, length of the jet

flight, diameter (circular jet) or thickness (nappe flow or rectangular jet) in impingement jet conditions, and water cushion depth. Annandale (1995, 2006) summarized and established a relationship between the stream power and the erodibility index for a wide variety of materials and flow conditions. Stream power per unit of area available of an impingement jet is:

$$P_{jet} = \frac{\gamma Q H}{A} \tag{12}$$

where γ is the specific weight of water, Q the flow, H the drop height or the upstream energy head, and A the jet area on the impact surface. The erodibility index is defined as:

$$K = M_s K_b K_d J_s \tag{13}$$

where M_s is the number of resistance of the mass, K_b the number of the block size, K_d the number of resistance to shear strength on the discontinuity contour, and J_s the number of structure relative of the grain.

The threshold of rock strength to the stream power, expressed in kW/m², is calculated and based on the erodibility index K.

$$P_{rock} = 0.48K^{0.44} \quad \text{if} \quad K \leq 0.1 \tag{14a}$$

$$P_{rock} = K^{0.75} \quad \text{if} \quad K > 0.1 \tag{14b}$$

Tables 6 and 7 show the formulae of the parameters and the values of the different variables considered and their respective calculus.

Table 6. Erodibility indexes parameters (adapted from Annandale, 2006).

Material	Formulae	Parameters
Rock	$M_s = 0.78 C_r UCS^{1.05} \quad when \quad UCS \leq 10 MPa$ $M_s = C_r UCS \quad when \quad UCS > 10 MPa$ $C_r = \dfrac{g\rho_r}{\gamma_r}$	UCS = unconfined compressive strength C_r = coefficient of relative density ρ_r = mass density of the rock g = gravity γ_r = reference unit weight of rock ($27 \cdot 10^3$ N/m³)
Non-cohesive granular soil	The relative magnitude is obtained by means of the standard penetration test (SPT). When the SPT value exceeds 80, the non-cohesive granular material is taken as rock.	
Rock	$K_b = \dfrac{RQD}{J_n}$	RQD = rock quality designation RQD = values range between 5 and 100 J_n = values range between 1 and 5 K_b = values range between 1 and 100 J_n = join set number
Non-cohesive granular soil	$K_b = 1000 D^3$	d = characteristic particle diameter
Rock	$K_d = \dfrac{J_r}{J_a}$	J_r = joint wall roughness number J_a = join wall alteration number
Non-cohesive granular soil	$K_d = tan\,\phi$	ϕ = residual friction angle of the granular earth material

Table 7. Semi-empirical methodology. Input and calculated values (Castillo and Carrillo 2016b).

Variable	Value
Angle of rock friction, SPT (º)	38
Specific weight (KN/m^3)	27.64
Unconfined compress. resistant, UCS (Mpa)	50
Relative density coefficient, C_r	1.024
RQD (calculated)	82.66
Number of join system (calculated), J_n	1.83
Discontinuity spacing, J_x, J_y, J_z (m)	0.5
Average block diameter (calculated), (m)	0.5
Roughness degree, J_r	2
Alteration degree, J_a	1

The dynamic pressure in the bottom of the stilling basin was calculated with the formulae (Eq. 1 to 4), tables (1 and 2 and figures (5a, 5b and 5c) presented in the Introduction.

Table 8 shows the results obtained in the three types of material existent in the place of the dam and considering a concrete slab of 20 MPa characteristic strength.

Table 8. Stream power of free surface jets for different flows as a function of the erodibility: alluvial, weathered rock, intact rock and concrete slab indexes (water cushion depth h_a = 24 m) (Castillo and Carrillo 2016b).

Variable	Alluvial	Weathered rock	Intact rock	Concrete
M_s	0.19	0.41	51.19	27.77
K_b	11.39	125	49.18	49.18
K_d	0.78	0.78	2.00	5.33
J_s	1.00	1.00	0.60	1.00
Erodibility index, K	1.69	40	3021	7280
Stream power, P_{rock} (kw/m^2)	1.50	16	408	788

In Figure 18 the stream power of the free surface weir jet is indicated, together with the power threshold of alluvial, weathered and intact rock. Considering a water cushion depth h_a = 24 m (tail water depth h = 6 m), the flow rate of 500 m^3/s would have the power to erode the weathered rock, although the design flow of 700 m^3/s, would not have enough power to reach the intact rock. These confirm that the maximum scour of the free surface weir could be near to D_s = 26 m (alluvial 24 m and weathered rock 2 m).

We can observe that the half-height outlet case does not correspond strictly with circular neither rectangular (nappe flow) jet case. For circular jets, the C_p and C_p' are valid for $H/L_b \leq 0.50$ (Ervine *et al.* 1997). However, for the design flow (Q_{40} = 1760 m^3/s) the H/L_b = 1.67. For this reason the calculus in Figure 18 were carried out by using the rectangular jet analogy.

The stream power threshold of weathered rock ($P_{weathered\_rock}$ = 16 kW/m^2) does not resist the flow of the annual return period (Q_{ma} = 136 m^3/s). The intact rock stream power (P_{rock} = 408 kW/m^2) could resist up to a flow return period of 5 years (Q_5 = 820 m^3/s). The Q_{10} = 1180 m^3/s would exceed the intact rock strength, while the design flow reach a significant scour in the intact rock. As a solution to the scour, a concrete slab of 20 MPa characteristic strength and thickness of 2 m (P_{conc} = 788 kW/m^2) is placed directly on the alluvial level (796 MASL).
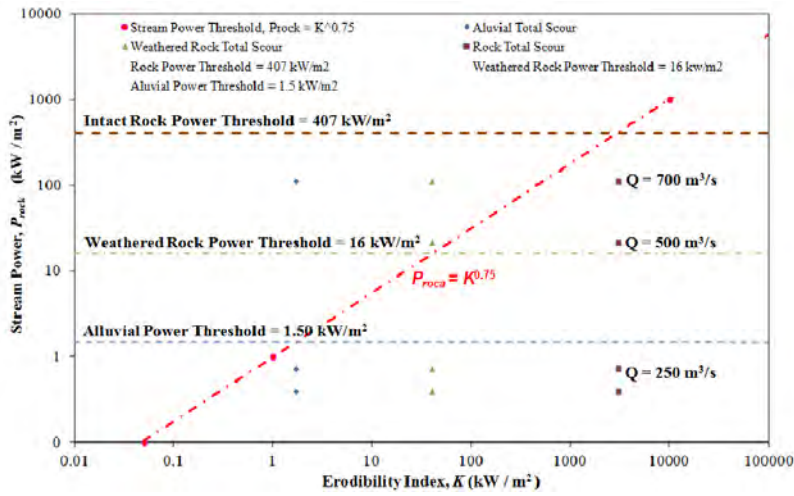
Figure 18. Stream power of the jet for different flows as a function of the erodibility. Alluvial, weathered rock and intact rock indexes ($h_a = Y = 24$ m, $h = 6$ m) for the free surface weir (Castillo and Carrillo 2016b).

The geometry of the pre-excavated basin should be similar to the geometry of the basin that would be formed with the flow $Q_{40} = 1766$ m^3/s. Figure 19 indicates that the concrete slab would resist the power stream of the design flow ($P_{jet} = 666$ kW/m^2).
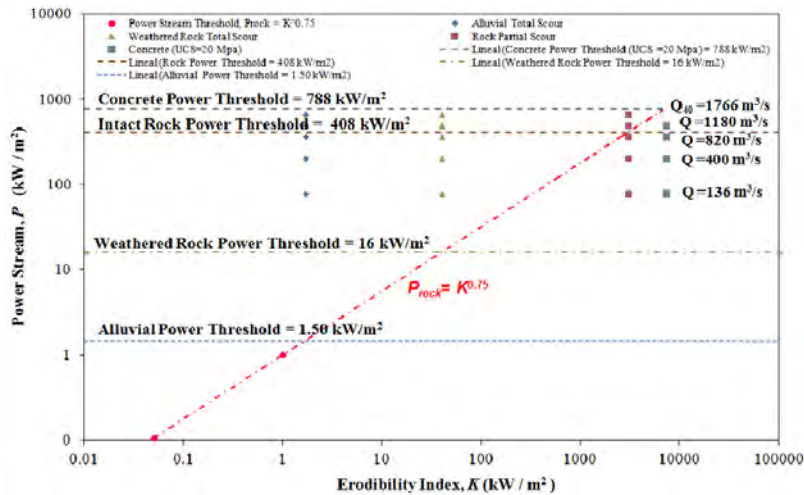
Figure 19. Stream power of the jet for different flows as a function of the erodibility. Alluvial, weathered rock and intact rock indexes ($h_a = Y = 24$ m, $h = 6$ m) for the half-height outlet (Castillo and Carrillo 2016b).

NUMERICAL SIMULATION

As a complement of the empirical and semi-empirical methodologies, we carried out three-dimensional mathematical model simulations. These programs allow a more detailed characterization and, thus, a detailed study of local effects of the sediments transport. We used the Computational Fluid Dynamics (CFD) program FLOW-3D. It solves the Navier-Stokes equations discretized by finite differences and incorporates various turbulence models, a sediment transport model (Meyer-Peter and Müller 1948) and an empirical model of bed erosion (Mastbergen and Von den Berg 2003); Brethour and Burnham 2010), together with a method for calculating the free surface of the fluid without solving the air component TrueVOF^{TM} (Hirt and Nichols 1981).

In order to simulate the proper functioning of the free surface weir, we carried out several simulations by means of sensibility analysis: air entrainment models, turbulence models, mesh size and type of solver, among others (Castillo and Carrillo 2013, 2014). We compared pressures obtained in the stagnation point and their associated mean dynamic pressure coefficients with the parametric methodology.

Principal data for the analysis were q = 19.44 m²/s and H = 120.00 m. With these data, the calculated impingement jet thickness was B_j = 1.46 m.

We obtained the most accurate results by using a mesh size of 0.2 m. In the solver options, we selected the stability and convergence method and the free surface solved with the split Lagrangian method. Table 9 compares the mean pressure and the mean dynamic pressure coefficient obtained by the non-effective water cushion case.

Table 9. Comparison of pressures and C_p, considering a water cushion h = 2 m
(Castillo and Carrillo 2013, 2014).

Variable	Parametric methodology	FLOW-3D
Net drop height (m)	120.00	120.00
Mean dynamic pressure (m)	30.56	33.44
Mean dynamic pressure coefficient, C_p	0.28	0.31

The sediment scour model of FLOW-3D estimates the motion of sediment flow by predicting the erosion, advection and deposition of sediment. This is done by considering two states in which sediment can exist: suspended and packed sediment. Suspended sediment is typically of low concentration and advects with fluid flow. Packed sediment exists in the computational domain at the critical packing fraction (we used value 0.70 considering the existing field data). Only a thin surface layer of grains of the packed sediment can move in the form of bed-load transport.

Suspended sediment is transported by advection along with the fluid. FLOW-3D assume there are totally N sediment species. The transport equation for each sediment species i is

$$\frac{\partial \boldsymbol{u}_{s,i}}{\partial t} + \overline{\boldsymbol{u}} \cdot \nabla \boldsymbol{u}_{s,i} = -\frac{1}{\rho_{s,i}} \nabla P_r + \boldsymbol{F} - \frac{K_i}{f_{s,i}\rho_{s,i}} \boldsymbol{u}_{r,i} \tag{15a}$$

$$\frac{\partial \overline{\boldsymbol{u}}}{\partial t} + \overline{\boldsymbol{u}} \cdot \nabla \overline{\boldsymbol{u}} = -\frac{1}{\overline{\rho}} \nabla P_r + \boldsymbol{F} \tag{15b}$$

where $\boldsymbol{u}_{s,i}$ is the velocity of sediment species i; $\rho_{s,i}$ the density of the sediment species i; $f_{s,i}$ the volume fraction of sediment species i; P_r the pressure; K_i the coefficient of quadratic drag for species i; $\boldsymbol{F}$ includes body and viscous forces; $\boldsymbol{u}_{r,i}$ is the relative velocity between the velocity ($\boldsymbol{u}_{s,i}$) of sediment species i and the fluid velocity ($\boldsymbol{u}_f$), and $\overline{\rho}$ is density of fluid-sediment mixture.

Subtracting Equation 15a from Equation 15b gives

$$\frac{\partial \boldsymbol{u}_{drift,i}}{\partial t} + \overline{\boldsymbol{u}} \cdot \nabla \boldsymbol{u}_{drift,i} = \left(\frac{1}{\overline{\rho}} - \frac{1}{\rho_{s,i}}\right) \nabla P_r + \boldsymbol{F} - \frac{K_i}{f_{s,i}\rho_{s,i}} \boldsymbol{u}_{r,i} \tag{16}$$

where $\boldsymbol{u}_{drift,i} = \boldsymbol{u}_{s,i} - \overline{\boldsymbol{u}}$ is the velocity needed to compute the transport of sediment due to drift. Assuming that the motion of the sediment is nearly steady at the scale of the computational time and that the advection term is small (i.e., for small drift velocity $\boldsymbol{u}_{drift}$), the result of Equation 16 is

$$\boldsymbol{u}_{r,i} = \frac{\nabla P_r}{\rho K_i}\left(\rho_{s,i} - \overline{\rho}\right)f_{s,i} \tag{17}$$

where K_i is the drag function and combines form drag and Stokes drag (Flow Science 2015). The correction to account for particle/particle interactions is an experimentally determined relation referred to as the Richardson-Zaki (1954) correlation. Table 10 shows the principal relations to calculate the sediment scour model in FLOW-3D.

Sediment is entrained by the picking up and re-suspension of packed sediment due to shearing and small eddies at the packed sediment interface. The empirical model used in FLOW-3D is based on Mastbergen and Von den Berg (2003). The first step to computing the critical Shields number is calculating the dimensionless parameter R_i^* and from this, the dimensionless critical Shields parameter $\theta_{cr,i}$ is computed using the Soulsby-Whitehouse equation (Soulsby 1997). The critical Shields parameter can be modified for sloping surfaces to include the angle of repose. The local Shields number is computed based on the local shear stress, τ. It is assumed that the Nikuradse roughness

of the bed surface is proportional to the local mean grain diameter in packed sediment: $k_s = c_{rough}\ d_{50,packed}$. We used the default value of the proportional constant $c_{rough} = 1.0$. The entrainment lift velocity of sediment is then computed with Mastbergen and Von den Berg expression and in function of the dimensionless particle diameter, d_* (see Table 10). The entrainment velocity $u_{lift,i}$ is then used to compute the amount of packed sediment that is converted into suspended sediment, effectively acting as a mass source of suspended sediment at the packed bed interface. Once converted to suspended sediment, the sediment subsequently advects and drifts.

Table 10. Principal relations to calculate the sediment scour model in FLOW-3D (Castillo and Carrillo 2016b).

Relation	Formulae	Parameters
Drag function	$K_i = \dfrac{3}{4}\dfrac{f_{s,i}}{d_{s,i}}\left(\rho_f C_{D,i}\|\mathbf{u_{r,i}}\| + 24\dfrac{\mu_f}{d_{s,i}}\right)$	$d_{s,i}$ and $C_{D,i}$ = diameter and drag coefficient for sediment species i
Drift velocity correction	$\mathbf{u_{r,i}^{eff}} = \mathbf{u_{r,i}}(1 - f_s)^{\zeta}$	μ_f = fluid dynamic viscosity $\mathbf{u_{r,i}}$ = drift velocity
Rchardson-Zaky coefficient	$\zeta_0 = 4.35/R_e^{0.03}$ for $R_e < 1.0$ $\zeta_0 = 4.45/R_e^{0.1}$ for $1.0 < R_e < 500$ $\zeta_0 = 2.30$ for $R_e > 500$	f_s = sediment total volume fraction $\zeta = \zeta_{user}\zeta_0;\ \zeta_{user} = 1$ $R_e = \rho_f d_i \|\mathbf{u_{r,i}}\|/\mu_f$ = Reynolds number on
Critical Shields parameter (S-W)[*]	$\theta_{cr,i} = \dfrac{0.3}{1 + 1.2R_i^*} + 0.055\left[1 - \exp(-0.02R_i^*)\right]$	the particle d_i ρ_f = fluid density
Critical Shields parameter modified for sloping surface	$\theta_{cr,i}' = $ $\theta_{cr,i}\dfrac{\cos\Psi\sin\beta + \sqrt{\cos^2\beta\tan^2\varphi_i - sen^2\Psi sen^2\beta}}{\tan\varphi_i}$	$R_i^* = d_{s,i}\dfrac{\sqrt{0.1(\rho_{s,i} - \rho_f)\rho_f\|g\|d_{s,i}}}{\mu_f}$ $\rho_{s,i}$ = density of sediment species i
Local Shields number	$\theta_i = \dfrac{\tau}{\|g\|d_{s,i}(\rho_{s,i} - \rho_f)}$	β = slope bed angle f$_i$ = repose angle for sediment species i (default is 32º)
Sediment entrainment lift velocity	$\mathbf{u_{lift,i}} = \alpha_i\mathbf{n}_s d_*^{0.3}\left(\theta_i - \theta_{cr,i}'\right)^{1.5}\sqrt{\dfrac{\|g\|d_{s,i}(\rho_{s,i} - \rho_f)}{\|g\|d\rho_f}}$	Ψ = angle between the flow and the upslope direction (flow directly up a slope $\Psi = 0$º)
Dimensionless particle diameter	$d_* = d_{s,i}\left[\dfrac{\rho_f(\rho_{s,i} - \rho_f)\|g\|}{\mu^2}\right]^{\frac{1}{3}}$	τ = local shear stress $\|g\|$ = gravitational vector α_i = entrainment parameter (~0.018)
Volumetric bed-load transport rate per unit width	$q_{b,i} = f_{b,i}\Phi_i\left[\|g\|\left(\dfrac{(\rho_{s,i} - \rho_f)}{\rho_f}\right)d_{s,i}^3\right]^{\frac{1}{2}}$	$\mathbf{n}_s$ = outward pointing normal to the packed bed interface $f_{b,i}$ = volume fraction of sediment i in the bed-load layer
Bed-load thickness	$\dfrac{\delta_i}{d_{s,i}} = 0.3d_*^{0.7}\left(\dfrac{\theta_i}{\theta_{cr,i}'} - 1\right)^{0.5}$	Φ_i = dimensionless bed-load transport (MPM)[**] d_* = dimensionless particle diameter θ_i = local Shields number

[*]Soulsby and Waithouse equation. [**]Meyer-Peter and Müller equation.

Bed-load transport is the sediment transport due to rolling or bouncing over the surface of the packed bed of sediment. The model currently used in FLOW-3D is from Meyer-Peter and Muller (1948). This model predicts the

volumetric flow of sediment per unit width over the surface of the packed bed:

$$\Phi_i = \beta_i(\theta_i - \theta'_{cr,i})^{1.5} \tag{18}$$

where the typical value of $\beta_i = 8$ (Van Rijn, 1984) and which has been used in our different simulations (5 and 13 for low and high sediment transport, respectively). Φ_i is related to the volumetric bed-load transport rate per unit width, q_{bi}. The bed-load thickness of the saltating sediment is estimated with Van Rijn (1984) relation (see Table 10). To compute the motion of the sediment in each computational cell, the value of $q_{b,i}$ is converted into a velocity by $u_{bedload,i} = q_{b,i}/\delta_i f_{b,i}$. The direction of the motion is determined from the motion of the liquid adjacent to the packed bed interface. Therefore, the volumetric flux is $u_{bedload,i} = u_{bedload,i}(\overline{u}/\|\overline{u}\|)$, where $(\overline{u}/\|\overline{u}\|)$ is the direction of the fluid-sediment mixture adjacent to the packed interface, and the resulting bed-load velocity, $u_{bedload,i}$, is used to transport the packed sediment.

Settling and entrainment of grains are opposite processes and often occur at the same time. In the 3D scour model, the settling velocity is related to the drift velocity near bed as $u_{settling,i} = -u_{drift,i} \cdot n_s$; where n_s is the outward pointing normal to the packed bed interface.

The model in FLOW-3D v.11 is fully coupled with fluid flow. The fundamental difference from the previous version is that the packed bed is described by the FAVOR[TM] technique. At each time step, area and volume fractions describing the packed sediments are calculated throughout the domain. However, the maximum size of the particle that can management this new version is over 35 mm (Flow Science 2015). For this reason, simulations were carried out in a Froude similitude scale 1:50 and the results transformed to prototype scale. The model had 4,159,233 cells and the scour reached the steady state after 60 seconds of simulation. With this setting, the time required to solve the problem was approximately 20.80 days in an Intel(R) Core(TM) i7-2600 CPU @3.40GHz processor and 24.0 GB RAM.

In Figure 20 we can observe the scour obtained with the CFD simulation. Scour depth was of 34 m (alluvial 24 m and weathered rock 10 m), which is greater than the calculated with the mean value of the empirical formulae (17 m) and to the semi-empirical methodology (~ 26 m).
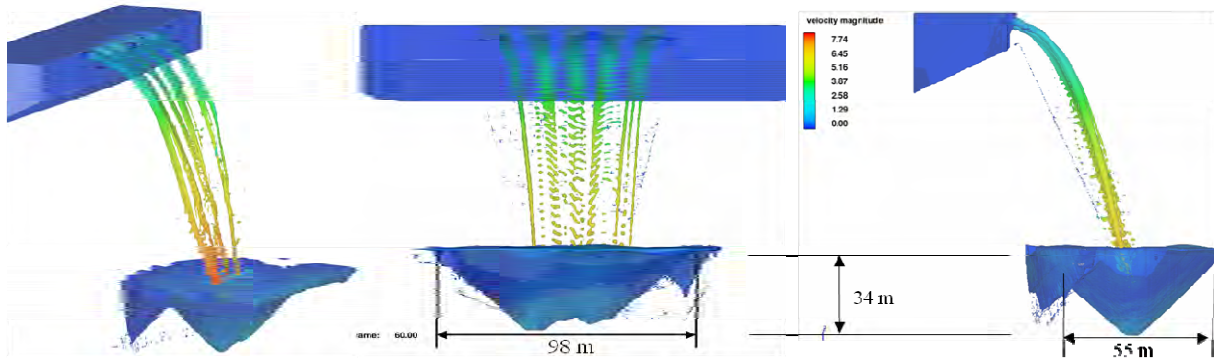
Figure 20. Scour basin due to free surface weir jet. Bilayer simulation: alluvial 24 m and weathered rock 10 m. Froude scale 1:50. Prototype impingement velocity = 6.1 x (50)$^{1/2}$ = 43.13 m/s (Castillo and Carrillo 2016b).

The scour is similar to the mean value + 1 standard deviation of the empirical formulae (34 m). However this value is a maximum threshold of scour because 1:50 scale modeling contains scale effects that are difficult to quantify.

To simulate of half-height outlet (two rectangular ducts of 5.00 x 5.80 m), the selection of the mesh size is function of their dimensions and of the thickness of the falling jets. Figure 21 shows the scour shape and size simulated considering bilayer material (alluvial 24 m and weathered rock 10 m).

The mesh consisted in hexahedral elements of 0.02 m (equivalent to 1.00 m in prototype scale using the Froude similitude). The inlet boundary condition considered the flow and the water height in the design condition, and outflow condition in the downstream condition. The domain consisted in 2,177,770 active cells. The time-step size

was controlled by stability and convergence criteria. Pressures obtained in the stagnation point and their associated mean dynamic pressure coefficients were compared with the parametric methodology. After 50 seconds of simulation (4.75E+06 seconds of CPU, 7.2 days of elapsed time), the maximum scour depth reached the intact rock (34 m). This value is a bit bigger than the obtained with the mean value adjustment of the empirical formulae (32 m), its equal to the mean value + 0.50 standard deviation (34 m) and a bit smaller than the semi empirical methodology whose value was greater than 34 m (alluvial 24 m, weathered rock 10 m and intact rock > 2 m).
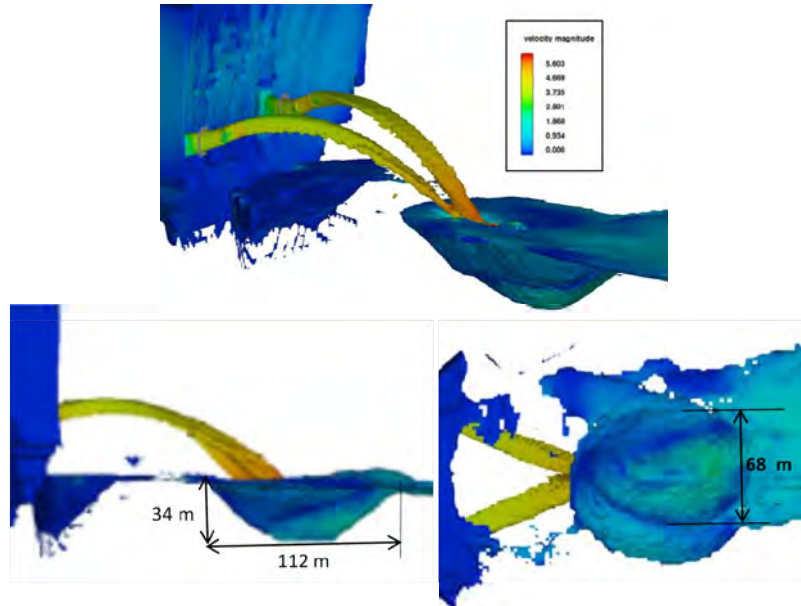
Figure 21. Scour basin due to the half-height outlet. Bilayer simulation: alluvial 24 m and weathered rock 10 m. Froude scale 1:50. Prototype impingement velocity = 5.4 x $(50)^{1/2}$ = 38.18 m/s (Castillo and Carrillo 2016b).

Table 11 summarizes the maximum scour obtained by the free surface weir and by the half height outlets when the design flow is considered.

Table 11. Comparison of scour obtained by different methods for free surface weir and half-height outlet (Castillo and Carrillo 2016b).

Method	Free Surface Weir			Half-height Outlet		
	Q_4 = 700 m^3/s			Q_{40} = 1760 m^3/s		
	D	$D + 0.50SD$	$D + SD$	D	$D + 0.50SD$	$D + SD$
	(m)	(m)	(m)	(m)	(m)	(m)
Empirical formulations	17	24	34	32	> 34	> 34
Erodibility Index –	26	-	-	> 34	-	-
Pressure fluctuations	(2 w.r.)[*]					
FLOW-3D v11	34	-	-	> 34	-	-

[*](2 w.r.) = 2 m in weathered rock.

For the empirical formulae, three values have been considered: the mean value (D), the mean value + 0.50 standard deviation $(D + 0.50 \, SD)$, and the mean value + standard deviation ($D + SD$). The scour obtained with the different methodologies are in agreement.

As far as the numerical simulation is concerned, the scour shape was analyzed considering the intact rock as non-

erodible. The upstream face of the scour occurred approximately 85 m downstream from the dam. The plant scour was near 112 m long and 68 m wide.

Considering the place of the dam, the scour would reach the left natural slope and it could cause landslides. A pre-excavated stilling basin shape has been proposed in order to adjusted to the geometry and the space available (Figure 22).
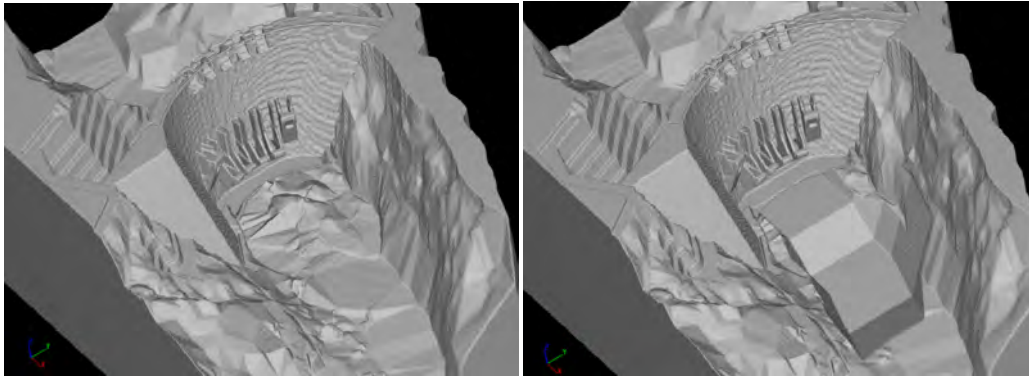
Figure 22. Pre-excavated basin. (**a**) Initial condition; (**b**) geometry proposed (Castillo and Carrillo 2016b).

In Figure 23 we can observe that the free surface weir jets are disintegrated in impingement conditions ($H/L_b = 1.31$ according to lab measurements). The velocities reach 43 m/s and are reduced until 6 m/s by diffusion in the water cushion. The instantaneous pressures on the bottom reach 28 m and correspond to hydrostatic pressure of the water cushion.
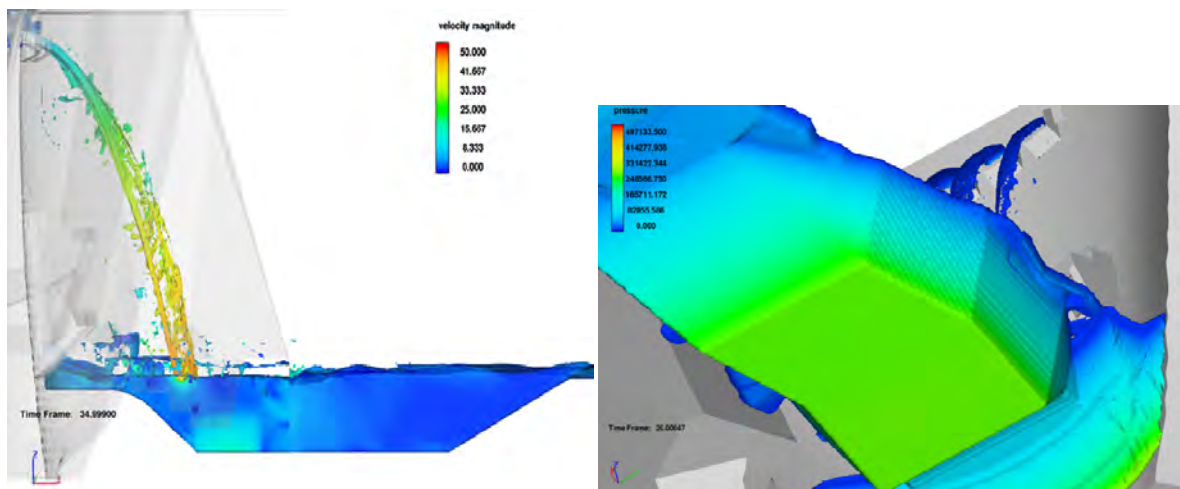
Figure 23. Lateral and spatial views of the free surface weir jets in the air and in the pre-excavated stilling basin: a) Velocities. b) Pressures ($Q = 700$ m^3/s) (Castillo and Carrillo 2016b).

For the half-height outlets, the velocities in spatial and lateral views are showed (Figure 24). The high velocity of the impingement jet is reduced by diffusion effect in the water cushion until 20 m/s. We can observe that there are very strong flow recirculation of vertical and horizontal axis. At the end of the pre-excavated stilling basin velocity is reduced to around 6 m/s.
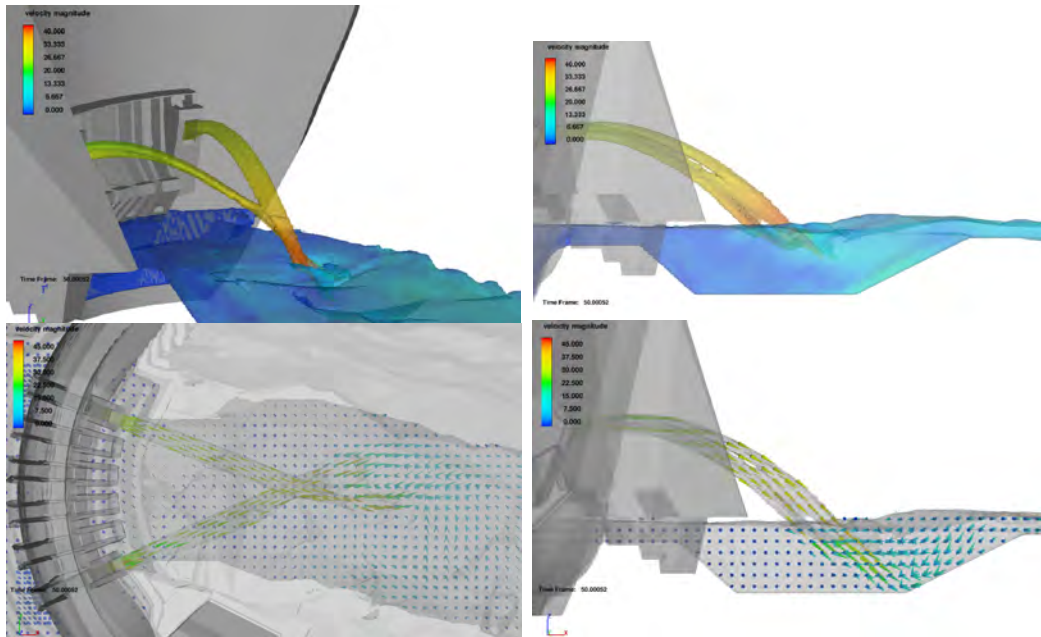
Figure 24. Spatial and lateral views of the flow velocity in the air and in the pre-excavated stilling basin (Castillo and Carrillo 2016b).

Figure 25 shows the total pressures in the pre-excavated stilling basin when the two ducts of half-height outlet are working (Q = 1760 m3/s) and when only one duct only is working (Q = 880 m^3/s), respectively.
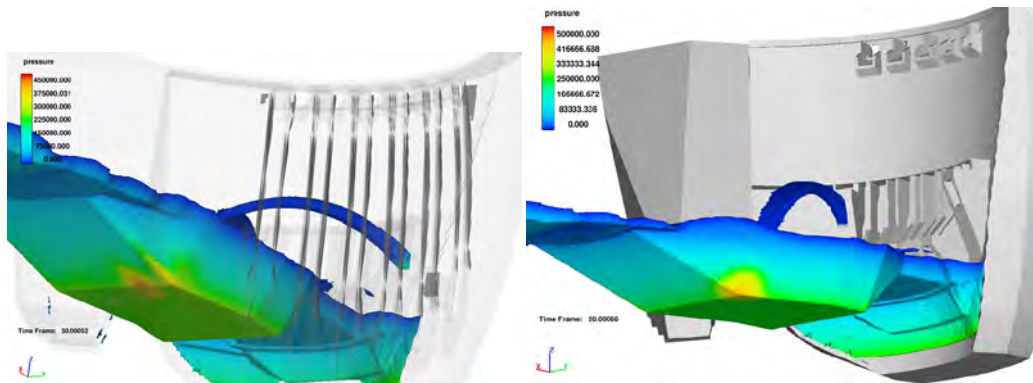
Figure 25. Spatial views of pressures in the pre-excavated stilling basin: (**a**) Working two ducts of half-height outlet (Q = 1760 m^3/s); (**b**) Working one duct of half-height outlet (Q = 880 m^3/s) (Castillo and Carrillo 2016b).

We can observe that when two ducts work, the total pressure reaches 45 m on the basin bottom. However, if one duct only working, then the pressure reaches 50 m. The reduction of 5 m of total pressure is due to the impact of the jets in the air (see Figure 24).

6.2. Toachi Dam

The Toachi Dam is located in the South-West of the city of Quito in Ecuador. It is a concrete dam with a maximum height of 59 m to the foundations. The top level has 10 m of thickness and a length of 170.5 m. It is located at an altitude of 973 meters above sea level. The upstream and downstream embankment side slopes are 0.3/1.0 and 0.7/1.0 (horizontal/vertical), respectively.

The reservoir collects water from the basins of the Toachi and Sarapullo rivers. It has a total volume of 8 hm^3 with normal maximum water level located at 973 meters. At this level, the reservoirs have a length of 1.3 km in the Sarapullo River and 3.2 km in the Toachi River.

The dam has two Creager spillways controlled by gates. The spillways end in a ski jump and they have two baffles to divide the flow. The design flow matches a 1000-year return period (1213 m^3/s) with an energy head of 7.50 m (Hidrotoapi, 2010). There are two bottom outlets whose combined capacity is 800 m^3/s. The dam also has a stepped spillway for the Sarapullo River with a design flow of 40 m^3/s (Figure 26).
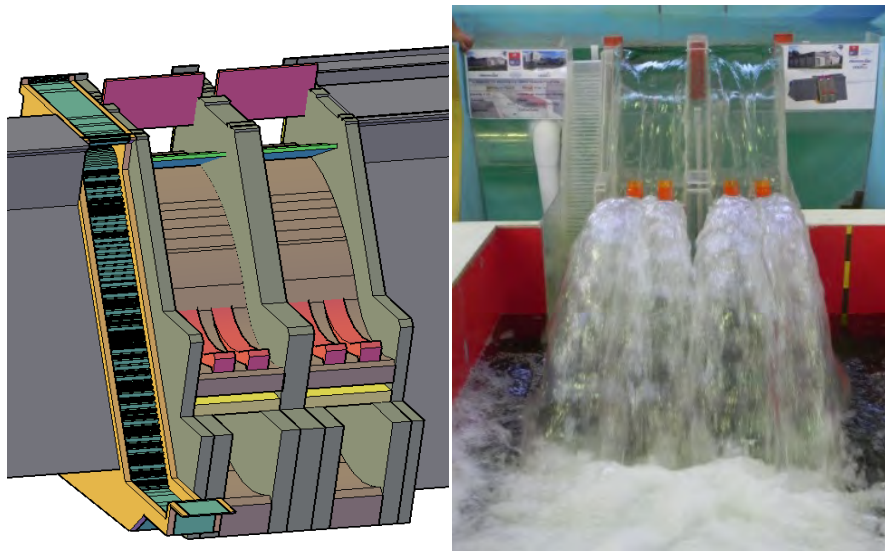
Figure 26. Three-dimensional view and physical model of the Toachi Dam (EPN 2013).

The rock-fill material has the following characteristics: Specific weight = 24 KN/m^3; internal friction of the granular material = 36º; Standard Penetration Test (SPT) = 80; d_{84} = material size in which 84% in weight is smaller = 1.20 m; d_{50} = material size in which 50% in weight is smaller = 1.02 m. The erodible layer is 10 m.

PHYSICAL MODEL SETUP

The physical model was built with a Froude scale 1:50 in the Centro de Investigaciones y Estudios en Recursos Hídricos (CIERHI) of the Escuela Politécnica Nacional (EPN), in Ecuador. To scale the surface roughness of the dam, the spillway was made of acrylic (Figure 27). For the study of pre-excavated stilling basin downstream of the dam, it was arranged a basin of 2.10 m long, 1.36 m wide and an erodible layer of 0.40 m deep. This basin was filled with a uniform crushed gravel size whose mean value was 0.020 m characteristic diameter (1.02 m in prototype). Downstream of the stilling basin, there are 0.20 m (10 m in prototype) of rock-fill joined by concrete before the transition to the Toachi River (EPN 2013).

Figure 27. 1:50 scale physical model of the Toachi ski jump (EPN 2013).

The scour downstream of the dam was analyzed by using different flows according to the hydrology report of the Toachi-Pilaton Dam (Hidrotoapi 2010). Each test was carried out during 90 minutes. After that time, researchers assumed that the scour had reached the equilibrium shape (EPN 2013). The scour generated a mound centered in the middle of the stilling basin, while the laterals maintained the original ground level. The maximum elevation of the mound was 0.90 m over the initial ground level.

Table 12 summarizes the maximum scour depth below the original bed (Y_s) and the distance from the dam to the maximum scour (D). The maximum scour $Y_s = 7.15$ m was obtained for the flow of 999 m³/s. The design flow (1213 m³/s) generated a bigger water cushion depth in the plunge pool (Y_0). Hence, the maximum scour depth for this flow (6.65 m) was smaller than with the smaller flow. The maximum scour distance, 64.20 m, was obtained with the design flow.

Table 12. Results obtained in the physical model (Castillo and Carrillo 2017).

Q_{model}	$Q_{protype}$	$Y_{s\ model}$	$Y_{s\ protopype}$	$Y_{0\ model}$	$Y_{0\ protopype}$	$Y_s + Y_{0\ model}$	$Y_s + Y_{0\ protopype}$	D_{model}	$D_{prototype}$
(l/s)	(m³/s)	(m)	(m)	(m)	(m)	(m)	(m)	(m)	(m)
14.95	264	0.131	6.57	0.110	5.47	0.241	12.05	1.035	51.75
28.26	500	0.161	8.05	0.155	7.75	0.316	15.80	1.219	60.95
40.21	711	0.141	7.05	0.174	8.68	0.314	15.70	1.282	64.10
56.51	999	0.143	7.15	0.245	12.25	0.388	19.40	1.233	61.65
68.63	1213	0.133	6.65	0.240	12.00	0.373	18.65	1.284	64.20

EMPIRICAL FORMULAE

Pagliara *et al.* (2004) compare the results of known formulae with their laboratory studies. They consider that several of the formulae are dimensionally incorrect. Another complication is the lack of the application ranges of these formulae. Following Castillo and Carrillo (2016b), 36 formulae have been examined. The formulae employed by several authors obtained from dimensional analysis may be expressed in a general expression:

$$D_s = Y_0 + Y_s = \Gamma \frac{q^x H^y Y_0^w}{g^v d_m^f d_{85}^h d_{90}^i} \tag{19}$$

where Y_0 is the tailwater depth, Γ an experimental coefficient, q the specific flow, H the energy head, g the gravity acceleration, d_m the average particle size of the bed material, d_{85} the bed material size in which 85% is smaller in weight, and d_{90} the bed material size in which 90% is smaller in weight. The principal variables are shown in Figure 28.

Figure 28. Scheme of scour in Toachi Dam (Castillo and Carrillo 2017).

Table 13 and 14 show the coefficients of 26 simplified scour formulae and 10 general scour formulae, respectively.

Table 13. Coefficients of 26 simplified scour formulae (Castillo and Carrillo 2017).

Author	Γ	x	y	c	v	f	h	i
Schoklitsch (1932)	0.521	0.57	0.2	0	0	0	0	0.32
Schoklitsch (1932)	4.75	0.57	0.2	0	0	0.32	0	0
Veronese-A (1937)	3.62	0.54	0.225	0	0	0.42	0	0
Veronese-B (1937)	1.9	0.54	0.225	0	0	0	0	0
Eggenburger (1944)	1.44	0.6	0.5	0	0	0	0	0.4
Hartung (1959)	1.4	0.64	0.36	0	0	0	0.32	0
Franke (1960)	1.13	0.67	0.5	0	0	0	0	0.5
Damle-A (1966)	0.652	0.5	0.5	0	0	0	0	0
Damle-B (1966)	0.543	0.5	0.5	0	0	0	0	0
Damle-C (1966)	0.362	0.5	0.5	0	0	0	0	0
Zimmerman & Maniak (1967)	0.59	0.2	0	0.93	0	0	0.23	0
Kotoulas (1967)	0.78	0.7	0.35	0	0	0	0	0.4
Chee & Padiyar (1969)	2.126	0.67	0.18	0	0	0.063	0	0
Bisaz & Tschopp (1972)	2.76	0.5	0.25	0	0	0	0	0.1
Chian Min Wu (1973)	1.18	0.51	0.235	0	0	0	0	0
Chee & Kung (1974)	1.663	0.6	0.2	0	0	0.1	0	0
Martins B (1975)	1.5	0.6	0.1	0	0	0	0	0
Taraimovich (1978)	0.633	0.67	0.25	0	0	0	0	0
Machado (1980)	1.35	0.5	0.3145	0	0	0	0	0.0645
SOFRELEC (1980)	2.3	0.6	0.1	0	0	0	0	0
INCYTH (1981)	1.413	0.5	0.25	0	0	0	0	0
Mason & Arumugam A (1985)	2.9	0.6	0.05	0.15	0.3	0.1	0	0
Mason (1989)	3.27	0.6	0.05	0.15	0.3	0.1	0	0
Suppasri (2007)	0.15	0.38	0.75	0	0	0	0	0
Heng *et al.* (2013)	7.4834	1.4652	-1.1978	0	0.7326	0	0	0

Table 14. Ten general scour formulae (Castillo and Carrillo 2017).

Author	Equation	Parameters
Jaeger (1939)	$Y_s + Y_0 = 0.6 q^{0.5} H^{0.25} (Y_0 / d_m)^{0.333}$	d_m = mean particle size of the bed material
Mikhalev (1960)	$Y_s + Y_0 = \dfrac{1.804\, q \sin \theta_j}{1 - 0.215 \cot \theta_j} \left(\dfrac{1}{d_{90}^{0.33} Y_0^{0.50}} - \dfrac{1.126}{H} \right)$	d_{90} = bed material size in which 90% in weight is smaller
Rubinstein (1963)	$Y_s + Y_0 = Y_0 + 0.19 \left(\dfrac{H_n + Y_0}{d_{90}} \right)^{0.75} \left(\dfrac{q^{1.20}}{H_n^{0.47} Y_0^{0.33}} \right)$	θ_j = impingement jet angle g = gravitational acceleration
Mirskhulava (1967)	$Y_s + Y_0 = \left(\dfrac{0.97}{\sqrt{d_{90}}} - \dfrac{1.35}{\sqrt{H_n}} \right) \dfrac{q \cdot \sin \theta_j}{1 - 0.175 \cdot \cot \theta_j} + 0.25 Y_0$	β = air-water relationship u_j = jet impact velocity at the tailwater surface
Martins-A (1973)	$\begin{cases} Y_s + Y_0 = 0.14 N - 0.73 \dfrac{Y_0^2}{N} + 1.7 Y_0 \\ N = \left(Q^3 H^{1.5} / d_m^2 \right)^{1/7} \end{cases}$	ρ = water density ρ_s = density of sediment q = specific flow
Mason & Arumugam (1985)	$Y_s + Y_0 = \left(6.42 - 3.10 H^{0.10} \right) \dfrac{g^{0.60 - (H/300)} H^{0.15 + (H/200)} Y_0^{0.15}}{g^{0.30} d_{50}^{0.1}}$	
Mason (1989)	$Y_s + Y_0 = 3.39 \dfrac{q^{0.60} (1 + \beta)^{0.30} Y_0^{0.16}}{g^{0.30} d^{0.06}}$	
Veronese modified (1994)	$Y_s + Y_0 = 1.90 h^{0.225} q^{0.54} \sin \theta_j$	
D'Agostino (1994)	$Y_s = \left(0.70 K_r + 0.58 \right) \left(0.94 q^{2/3} - 1.60 d_{90} \right)$	
Bombardelli & Gioia (2006)	$Y_s + Y_0 = K \dfrac{q^{0.67} H^{0.67}}{g^{0.33} d^{0.33}} \left(\dfrac{\rho}{\rho_s - \rho} \right)$	

Figure 29 shows the results obtained with the 36 formulae at prototype scale.
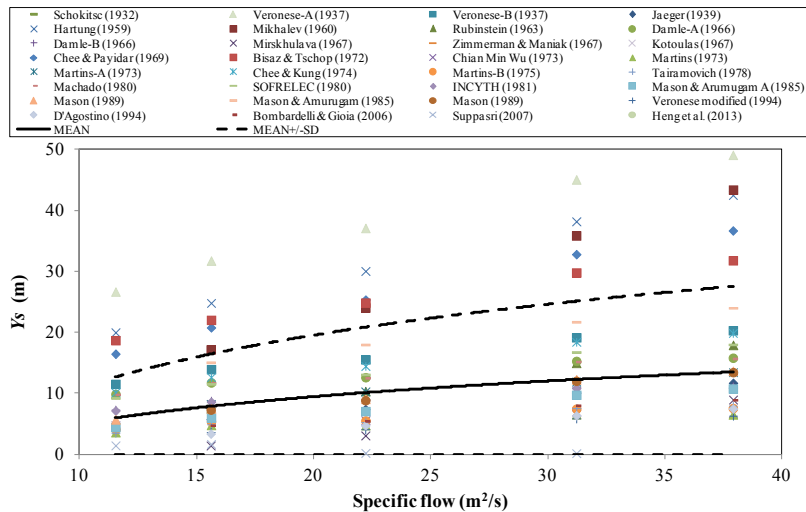
Figure 29. Scour of the ski jump obtained with 36 formulae and the threshold of +/- 1 standard deviation (Castillo and Carrillo 2017).

After removing those formulae with values that fall beyond the +/-1 standard deviation threshold, Figure 30 shows the mean value +/- 1 standard deviation values obtained, together with the scale model results. From the simplified expression, Damle-B (1966), Chian Min Wu (1973), Martins (1973), Martins-B (1975), Taraimovich (1978), INCYTH (1981), and Mason & Arumugam A (1985) are the formulae whose values are closest to the mean value. From the general expressions, Jaeger (1939), Mirskhulava (1967), Veronese modified (1994), D'Agostino (1994), and Bombardelli & Gioia (2006) are the formulae with values in the same range. If the mean value for the design flow (1213 m^3/s) were considered, the scour could reach a depth of 7.95 m. However, if the mean value +0.50 standard deviation were taken into account, then the same flow would scour 11.50 m. The values obtained in the physical model fall in the mean value +/- 1 standard deviation and are quite similar to the mean values calculated.
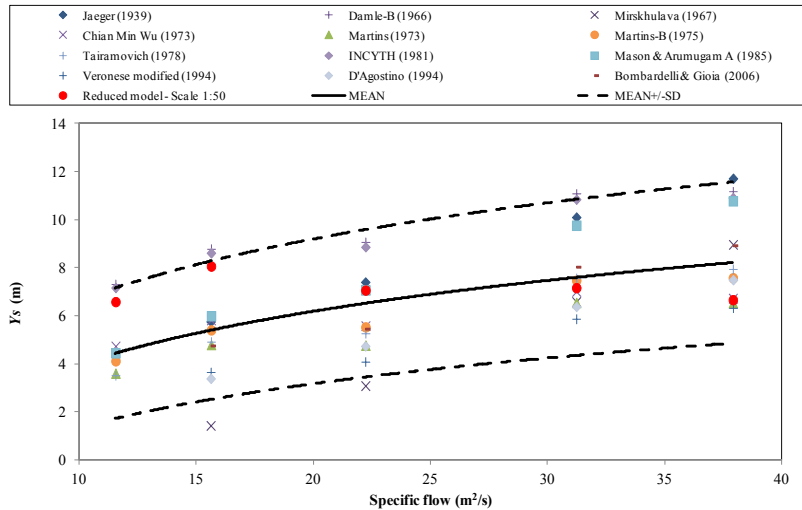
Figure 30. Scour of the ski jump obtained with the formulae in the threshold of +/- 1 standard deviation (Castillo and Carrillo 2017).

SEMI - EMPIRICAL FORMULAE

Table 15 shows the results obtained in the material located in the dam site, while Table 16 lists the results of the impingement stream (P_{jet}) and the diffused jet power by the water cushion ($P_{jet}/Y/B_j$) for several return period flows.

Table 15. Parameters of the threshold of rock strength (Castillo and Carrillo 2017).

d_{50}	d_{84}	θ	M_s	K_b	K_d	J_s	K	P_{rock}
(m)	(m)	(º)	(-)	(-)	(-)	(-)	(-)	(kW/m^2)
1.02	1.2	36	0.41	1061.21	0.73	1.00	316.12	74.97

Table 16. Impingement stream power (P_{jet}) and reduced stream power by diffusion in the water cushion [P_{jet} (Y/B_j)] (Castillo and Carrillo 2017).

Q	Y_s	Y_0	Y_0+Y_s	P_{jet}	P_{jet} (Y/B_j)
(m^3/s)	(m)	(m)	(m)	(kW/m^2)	(kW/m^2)
264	6.57	5.47	12.05	76.94	3.72
500	8.05	7.75	15.80	94.26	19.79
711	7.05	8.68	15.70	101.59	43.6
999	7.15	12.25	19.40	113.02	71.5
1213	6.65	12.00	18.65	108.31	64.59

Figures 31 and 32 show the stream power of the jet, together with the power threshold for the material located in the dam site. All flow rates impinge with enough power stream to erode a material with a power threshold of 74.97 kW/m^2. However, the stream power of the jet is reduced by diffusion in the water cushion. Considering the maximum scour depth measured in the laboratory model ($Y_0 + Y_s$), all the flows have a power threshold below the resistance of the material (74.97 kW/m^2). In this way, the results obtained with the semi-empirical formulae are in agreement with the data obtained in the scale model.
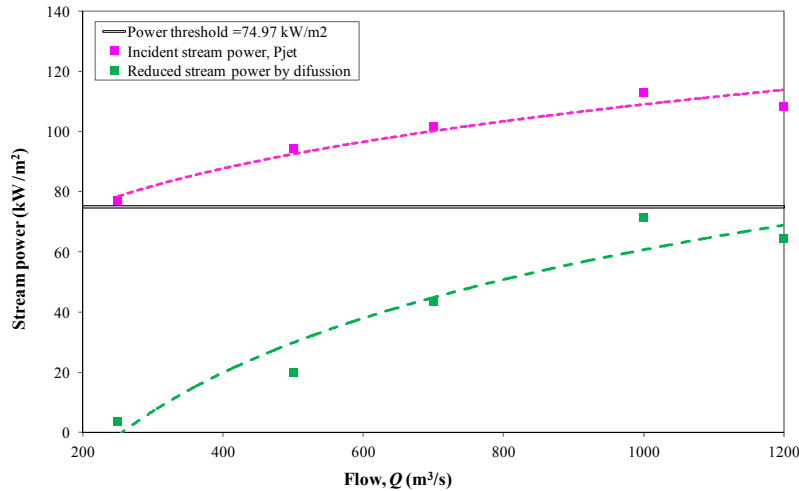
Figure 31. Incident stream power P_{jet} and reduced stream power by diffusion P_{jet} (Y/B_j) of the jet (Castillo and Carrillo 2017).
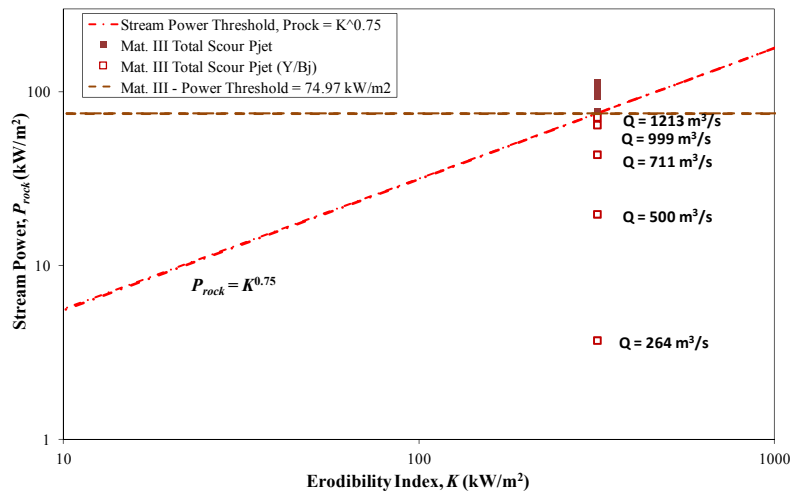
Figure 32. Stream power of the jet for different flows as a function of the erodibility (Castillo and Carrillo 2017).

NUMERICAL MODEL

A mesh size analysis was considered. For instance, the flight was simulated with a mesh size of 0.005 m and 0.004 m. Differences in the flight length were smaller than 0.5%, and the change in the water velocity was smaller than 0.07%. However, the required computational time to solve the same simulation with the finer mesh increased in 2.8 times.

After several tests, different mesh sizes were used in the model: 0.02 m for the reservoir and the plunge pool, 0.01 m for the beginning of the spillway, and 0.005 m for the final part of the spillway and the flight of the jets. Coarser

meshes showed discontinuities in the solid-water and in the air-water surfaces. Finer meshes did not show significance differences in the results but they increased the computational times. The selected mesh size distribution also allowed to obtain accurate mean dynamic pressure coefficient values in the stagnation point of the plunge pool when data were compared with laboratory measurements (Castillo *et al.*, 2015).

The model boundary conditions have been obtained from the scale model. The inlet and outlet boundary conditions are located far enough to not disturb the flow in the study area. They corresponded to the flow and the upstream and downstream water levels measured in the laboratory tests. Hydrostatic pressures distributions have been considered in both boundaries. For the walls of the upper deposit and the weir, no slip wall conditions and smooth walls have been considered to reproduce the surface roughness of the laboratory model.

The numerical simulation of the hydraulic behavior and scour by the action of the ski jump was analyzed. Considering previous works in other dams (Castillo and Carrillo 2016b), several simulations were carried out by means of sensitivity analysis: air entrainment models, turbulence models, grid size and type of solver, among others. Simulations were performed at laboratory scale. Figure 33 shows the three-dimensional view of the scour obtained for the design flow ($Q = 1213$ m³/s).
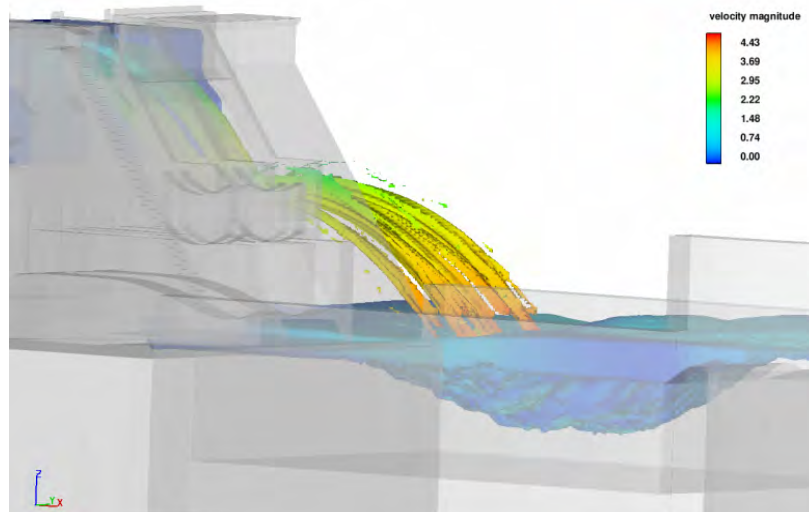
Figure 33. Velocities magnitude of the flow and scour downstream of the
Toachi Dam for the design flow ($Q = 1213$ m³/s) (Castillo and Carrillo 2017).

In the sediment scour model, the critical Shields number was calculated using the Soulsby-Whitehouse equation, while the Meyer-Peter & Müller equation was used to compute the bed load transport rate. Several bed load coefficients and turbulence models were analyzed and compared with the laboratory data and the empirical formulae.

Figure 34 shows the maximum scour (Y_s) results obtained for an intermediate flow (711 m³/s) and the design flow (1213 m³/s). The choice of the turbulence model and the bed load coefficient (β) had a significant impact on the results. For the k-ω turbulence model in the intermediate flow, the bed load coefficient had little effect and simulations obtained scour depths greater than those measured in the laboratory and calculated with the formulae. For the design flow, the tendency was changeable and the biggest scour was obtained with the intermediate bed load coefficient. The k-ε model tended to overestimate the scour when the bed load coefficient was small and a reduced scour for coefficients greater than 8. The choice of the RNG k-ε turbulence model and bed load coefficient lower than 6.5 obtained the results closest to the laboratory data and to the empirical formulae in both flows.
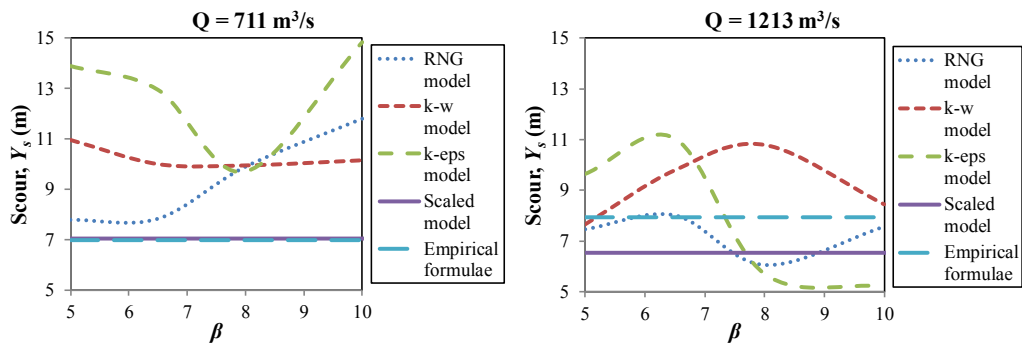
Figure 34. Comparison of the maximum scour downstream of the
Toachi Dam (Castillo and Carrillo 2017).

Figure 35 shows the comparison of the horizontal distance from the dam to the point in which the maximum scour depth is produced. The choice of the turbulence model and the bed load coefficient seem to have importance. For the intermediate flow, the RNG turbulence model obtains distances around 5% smaller than in the laboratory, whilst the other two turbulence models are closer when the smaller bed load coefficient is considered. For the design flow, the best results are obtained with the RNG and the k-ω turbulence models when $\beta < 7$.
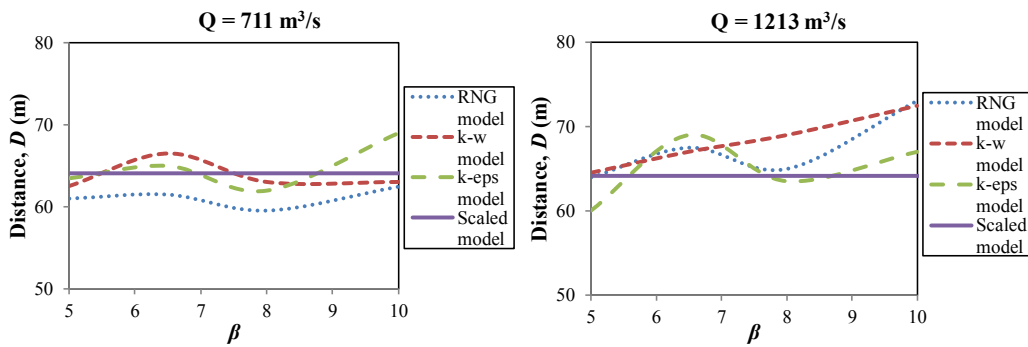
Figure 35. Numerical simulation of the scour downstream of the Toachi Dam (Castillo and Carrillo 2017).

Figure 36 compares the scour shape measured in laboratory with the numerical simulations calculated with the RNG k-ε turbulence model in the longitudinal planes in which the maximum scour value was obtained. The horizontal distances from the dam to the maximum scour depth were 64.0 m ($\beta = 5.0$) and 67.5 m ($\beta = 6.5$), similar to the value of 64.20 m obtained in the laboratory. The longitudinal scour length from the laboratory data was around 51.55 m while the simulated value was 49 m. The transversal scour length was nearly the complete transversal section.
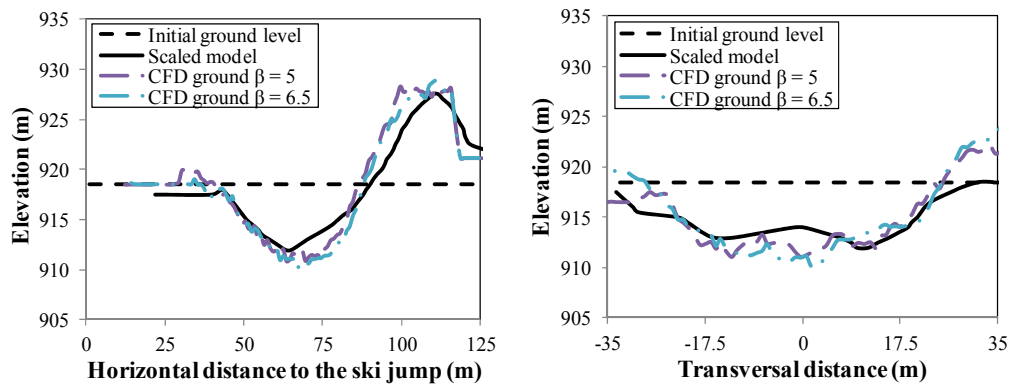
Figure 36. Longitudinal and transversal scour shape measured and simulated (Castillo and Carrillo 2017).

7. CONCLUSIONS

Observing and predicting two-phase flows in hydraulic structures is very complicated due to the rather non-dilute nature of the flow. Under non-dilute conditions, both experiments and simulations cannot be expected to lead to clean comparisons. Mean velocity and turbulent kinetic energy profiles have been analyzed in a plunge pool located downstream of a rectangular free-falling jet. In general, the CFD simulations provided results fairly close to the values measured in the laboratory, and to the formulas proposed by diverse authors, in spite of having used a simple two-phase flow model. "Homogeneous" model seems to be able to predict rather well areas in which air concentration is not very high. However, in the highly aerated regions rather strong differences appear. It was possible to propose a single mean velocity distribution law for ratios $V_x/V_{max} \geq 0.40$. For smaller values, there are necessarily diverse distribution laws.

On the other hand, similar results have been obtained by solving the problem from several perspectives and compared with a physical model: empirical formulations, erosion potential semi-empirical formulation and CFD simulations. This procedure allows to obtain a better and wider application of the state of the art.

Empirical formulae are traditionally used to estimate the maximum scour depth. However, they were obtained from different authors and tests. Their results are limited to their applicability range and there are important differences between one and other formula. Semi-empirical formulations consider the erosive potential of the material. However, the dissipation mechanisms in the air and in the plunge pool are not well known. Further studies are required to improve the knowledge of the hydrodynamics actions generated in the plunge pool and how the scour process is developed. In the numerical simulations, the choice of the turbulence model and of the bed load coefficient in the Meyer-Peter and Müller formula are of great importance. The maximum scour depth may vary up to the double as a function of these parameters. The best results were obtained using the RNG k- ε turbulence model and a bed load coefficient below 7. Three-dimensional numerical simulations of scouring processes involve high computational efforts. They require a calibrating procedure of the main parameters and to contrast the principal results with another source. Besides this, it is also necessary to improve the air-entrainment, turbulence and sediment transport models to solve the problem with a great deal of accuracy. As each method has its limitations, the results demonstrate the suitability of crossing methodologies to solve complex phenomena. Thus, numerical simulations were used to complement the laboratory measurements and the analytical approaches, allowing a better understanding of the physical phenomena in order to obtain an adequate solution. Considering the results obtained with the different methodologies, the pre-excavated stilling depth seems to be enough to ensure the formation of a stable plunge pool.

The designer has to take into account that results obtained with the reduced model and that the numerical simulations have scale effects. However, these results err on the side of caution.

8. REFERENCES 2

Adrian, R.J., and Westerweel, J. (2010). Particle Image Velocimetry. Cambridge University Press: Cambridge, UK.
Aki, S. (1969). Study on fluctuating characteristics of water dynamic force acting on base of free overfall. CRIEPI Research Report No. 69009 [in Japanese].
Annandale, G.W. (1995). "Erodibility". *J. Hydraulic Res.*, 33 (4), 471–494.
Annandale, G.W. (2006). Scour Technology. McGraw-Hill Professional, NY, USA.
ANSYS, Inc. (2015). *ANSYS CFX. Reference Guide. Release 16.0.*
Bercovitz, Y., Lebert, F., Jodeau, M., Buvat, C., Violeau, D., Pelaprat, L. and Hajczak, A. (2016). "LS-PIV procedure applied to a plunging water jet issuing from an overflow nappe." *Proceedings of the 4th IAHR Europe Congress. Sustainable Hydraulics in the Era of Global Change,* Liege, Belgium, 166–173.
Bollaert, E.F.R. and Schleiss, A.J. (2003). "Scour of rock due to the impact of plunging high velocity jets Part I: A state-of the-art review." *J. Hydraulic Res.,* 41(5), 451-464.
Bombardelli, F.A. and Gioia, G. (2006). "Scouring of granular beds by jet-driven axisymmetric turbulent cauldrons". *Phys. Fluids*, 18 (8), 088–101.
Bombardelli, F.A. and Jha, S.K. (2009). "Hierarchical modeling of the dilute transport of suspended sediment in open channels." *Environmental Fluid Mechanics,* 9, 207-235.

Brethour, J. and Burnham, J. (2010). Modeling Sediment Erosion and Deposition with the FLOW-3D Sedimentation and Scour Model; Flow Science Technical Note, FSI-10-TN85; Flow Science, Inc.: Santa Fe, Mexico; pp. 1-22.

Carrillo, J.M. (2014). Metodología numérica y experimental para el diseño de los cuencos de disipación en el sobrevertido de presas de fábrica. PhD Thesis. Departamento de Ingeniería Civil, Universidad Politécnica de Cartagena, Spain. [in Spanish].

Carrillo, J.M. and Castillo, L.G. (2014). "Laboratory measurements and numerical simulations of overtopping nappe impingement jets." *Dam Protections against Overtopping and Accidental Leakage - Proceedings of the 1st International Seminar on Dam Protections Against Overtopping and Accidental Leakage*, Madrid, Spain.

Carrillo, J.M., Castillo, L.G., Marco, F. and García, J.T. (2018). "Characterization of two-phase flows in plunge pools". 7º *International Symposium on Hydraulic Structures,* Aachen, Germany.

Castillo, L.G. (1989). Metodología experimental y numérica para el diseño de los cuencos de disipación de energía. Aplicación al vertido en presas bóveda. PhD Thesis. Departamento de Ingeniería Hidráulica, Marítima y Medio Ambiental, Universidad Politécnica de Cataluña, Spain. [in Spanish].

Castillo, L.G. (2006). "Aerated jets and pressure fluctuation in plunge pools". *Proceedings of the 7th International Conference on Hydroscience and Engineering*, Philadelphia, USA.

Castillo, L.G. and Carrillo, J.M. (2013). "Analysis of the scale ratio in nappe flow case by means of CFD numerical simulation." *Proc. 35th IAHR World Congress*, Chengdu, China.

Castillo, L.G., Carrillo, J.M. and Sordo-Ward, A. (2014). "Simulation of overflow nappe impingement jets." *Journal of Hydroinformatics*, 16(4), 922-940.

Castillo, L.G. and Carrillo (2014). "Characterization of the dynamics actions and scour estimation downstream of the dam". *Dam Protections against Overtopping and Accidental Leakage - 1st International Seminar on Dam Protections Against Overtopping and Accidental Leakage*, CRC Press 2015, pp. 231–243. Madrid, Spain.

Castillo, L.G., Carrillo, J.M. and Blázquez, A. (2015). "Plunge pool dynamic pressures: a temporal analysis in the nappe flow case." *J. Hydraulic Res.*, 53(1), 101-118.

Castillo, L.G. and Carrillo (2016a). "Pressure and velocity distributions in plunge pools". *2º International Seminar on Dam Protections Against Overtopping and Accidental Leakage*, Ft. Collins, Colorado, USA.

Castillo, L.G. and Carrillo (2016b). "Scour, velocities and pressures evaluations produced by spillway and outlets of dam". *Water*, 8, 68; doi:10.3390/w8030068.

Castillo, L.G., Carrillo, J.M. and Bombardelli, F.A. (2017). "Distribution of mean flow and turbulence statistics in plunge pools." *Journal of Hydroinformatics*, 19(2), 173-190.

Castillo, L.G. and Carrillo, J.M. (2017). "Comparison of methods to estimate the scour downstream of a ski jump". *International Journal of Multiphase Flow*". 92, 171-180.

Cola, R. (1966). Diffusione di un getto piano verticale in un bacino d'aqua d'altezza limitata. *L'Energia Elettrica*, *11*, 649–667 [in Italian].

Chee, S.P. and Padiyar, P.V. (1969). "Erosion at the base of flip buckets". *Eng. J. Inst. Canada* 52 (111), 22–24 .

Damle, P.M. , Venkatraman, C.P. and Desai, S.C. (1966). "Evaluation of scour below ski jump buckets of spillways". *In: Proc., Golden Jubilee Symp*, 1. Poona, India. Central Water and Power Res. Station, pp. 154–163.

D'Agostino, V. (1994). "Indagine sullo scavo a valle di opera transversai mediante modello fisico a fondo mobile". *L'Energía Elettrica* 71 (2), 37–51 (in Italian).

Drew D. A. and Passman S. L. (1999). "*Theory of Multicomponent Fluids.*" Applied Mathematical Sciences. Volume 135. Springer New York.

Ervine, D.A. and Falvey, H.R. (1987). "Behaviour of turbulent water jets in the atmosphere and plunge pools." *Proc. Int. Conf. Institutions of Civil Engineers*, 83(2), 295-314.

Ervine, D. A., Falvey, H. T. and Withers, W. A. (1997). "Pressure fluctuations on plunge pool floors." *J. Hydraul. Res.,* 35(2), 257–279.

Escuela Politécnica Nacional, HIDROTOAPI E.P. (2013). Estudio experimental en modelo hidráulico. Escala 1:50. Verificación experimental del diseño definitivo de la presa Toachi y obras complementarias. Informe Técnico Fase IV. Quito, Ecuador.

FEMA (2014). Technical Manual: Overtopping Protection for Dams. Federal Emergency Management Agency. FEMA P-1014, May. US Department of Homeland Security. USA.

Federspiel, M.P.E.A. (2011). Response of an embedded block impacted by high-velocity jets. PhD Thesis, nº 5160, École Polytechnique Fédérale de Lausanne, Suisse.

Flow Sciences Inc. (2015). *FLOW-3D Users Manual Version 11.1*. Santa Fe, New Mexico.

Frizell, K.W. (2000). Effects of aeration on the performance of an ADV. *In: 2000 Joint Conf. on Water Resources Engineering and Water Resources Planning & Management*. ASCE. Hotchkiss, R.H., Glade, M. (Eds.), Minneapolis, USA (CD-ROM).

Hidrotoapi, E.P. (2010). Informe 6256.0-R-18. Presa Toachi. Hidráulica. Memoria de cálculo Quito.

Jaeger, C. (1939). Uber die Aehnlichkeit bei flussaulichen Modellversuchen. Wasserkr. Wasserwirtsch. **1939**, 34, 269. (In German).

Machado, L.I. O (1982). Sistema de Dissipacao de Energia Proposto para a Barragem de Xingo. In Transactions of the International Symposium on the Layout of Dams in Narrow Gorges; ICOLD: Rio de Janeiro, Brazil.

Martins, R. (1973). "Contribution to the knowledge on the scour action of free jets on rocky river beds". *Proceedings of the 11th Congress on Large Dams*, Madrid, pp. 789-814.

Martins, R. (1975). "Scouring of rocky riverbeds by free-jet spillways". *Water Power Dam Const*. April.

Mason, P.J. and Arumugan, K. (1985). "Free jets scour below dams and flip buckets". *J. Hydraulic Eng.* 111 (2), 220–235.

Mason, P.J. (1989). "Effects of air entrainment on plunge pool scour". *J. Hydraulic Eng*. 115 (3), 385–399 .

Mastbergen, D.R. and Von den Berg, J.H. (2003). "Breaching in fine sands and the generation of sustained turbidity currents in submarine canyons". *Sedimentology* 50, 625–637.

Matos, J., Frizell, K.H., Andre, S. and Frizell, K.W. (2002). On the performance of velocity measurement techniques in air-water flows. *In: Hydraulic Measurements and Experimental Methods Conference 2002*. ASCE. Wahl, T.L., Pugh, C.A., Oberg, K.A. and Vermeyen, T.B. (Eds.). Estes Park, CO, USA.

Menter, F.R. (1994). "Two-equation eddy-viscosity turbulence models for engineering applications." *AIAA J.,* 32(8), 1598-1605.

Meyer-Peter, E. and Müller, R. (1948). "Formulas for bed-load transport". *In: Proceedings of the 2nd Meeting of the International Association for Hydraulic Structures Research*, pp. 39–64.

Mirtskhulava, T.E. (1967). "Alguns Problemas da Erosao nos Leitos dos Rios". Moscow. Trans. No 443do L.N.E.C. (in Portuguese).

Ohtsu, F., Yasuda, Y. and Awazu, S. (1990). Free and submerged hydraulic jumps in rectangular channels. Report of the Research Institute of Science and Technology. Nihon University. No 35.

Pagliara, S., Hager, W.H., and Minor, H.E. (2004). "Plunge pool scour in prototype and laboratory". *In: Hydraulics of Dams and River Structures*. Proceedings of the International Conference. Tehran, Iran, pp. 165–172.

Pope, S. B. (2000). Turbulent flows. Cambridge University Press.

Puertas, J. (1994). Criterios Hidráulicos para el diseño de cuencos de disipación de energía en presas bóveda con vertido libre por coronación. PhD Thesis. Universidad Politécnica de Cataluña, Spain (in Spanish).

Richardson, J.F. and Zaki, W.N. (1954). "Sedimentation and fluidization (Part I)". *Trans. Inst. Chem. Eng.* 32, 35-53.

Rodi, W., Constantinescu, C. and Stoesser, T. (2012). Large-Eddy Simulation in Hydraulics. IAHR Monograph, CRC Press.

Rouse, H. (1936). Discharge Characteristics of the Free Over Fall (Rouse, Civil Engineering).

Rubinstein, G.L. (1963). "Laboratory investigation of local erosion on channel beds below high overflow dams". *Transactions of Coordination Conferences on Hydraulic Engineering*. 1ss. VII, Conference on Hydraulics of High Head Water Discharge Structures Gosenergoizdat M.L.

Schoklitsch, A. (1932). Kolkbildung unter Über-fallstrahlen. Wasserwirtschaft, 25, 341–343. (In German).

Scimemi, E. (1930). "Sulla Forma delle Vene Tracimanti." *L'Energia Elettrica*, 7(4), 293-305. (in Italian).

Soulsby, R. (1997). "Chapter 9: Bedload transport. Dynamics of Marine Sand". *Thomas Telford Publications*, London, UK.

Stutz, B. and Reboud, J. L. (1997). "Two-phase flow structure of sheet cavitation." *Phys. Fluids,* 9(12), 3678–3686.

Suppasri, A. (2007). Hydraulic Performance of Nam Ngum 2 Spillway; Asian Institute of Technology: Pathumthani, Thailand.

Taraimovich, I.I. (1978). "Deformation of channels below high head spillways on rock foundations". *Hydrotech. Constr*. 9, 917–922.

Thielicke, W., and Stamhuis, E. (2014). "PIVlab–towards user-friendly, affordable and accurate digital particle image velocimetry in MATLAB." *Journal of Open Research Software*, 2(1).

Van Rijn, L. (1984). "Sediment transport, Part I: bed load transport". *J. Hydraul. Eng*. 110, 1431–1456.

Veronese, A. (1937). Erosioni di fondo a valle di uno scarico. Ann. Lavori Pubblici, 75, 717–726. (In Italian)

Wahl, T.L., Frizell, K.H. and Cohen, E.A. (2008). "Computing the trajectory of free jets." *J. Hydraul. Eng.,* 134(2), 256-260.

Wu, S. and Rajaratnam, N. (1996). "Free jumps, submerged jumps and wall jets." *J. of Hydraulic Research*, 33(2), 197-212.

Xu Duo-Ming, and Yu Chang-Zhao (1983). Pressures on the bottom of a channel due to the impact of a plane jet and their fluctuant characteristics. *Shuili xuebao*, Beijing, *5*, 52–58 [in Chinese].